12

CERL

US Army Corps
of Engineers
Construction Engineering
Research Laboratory

TECHNICAL REPORT M-345
May 1984

AN INVESTIGATION INTO POLYMER DESIGN AND SYNTHESIS FOR INFRARED ENERGY ABSORPTION

by
Alvin Smith

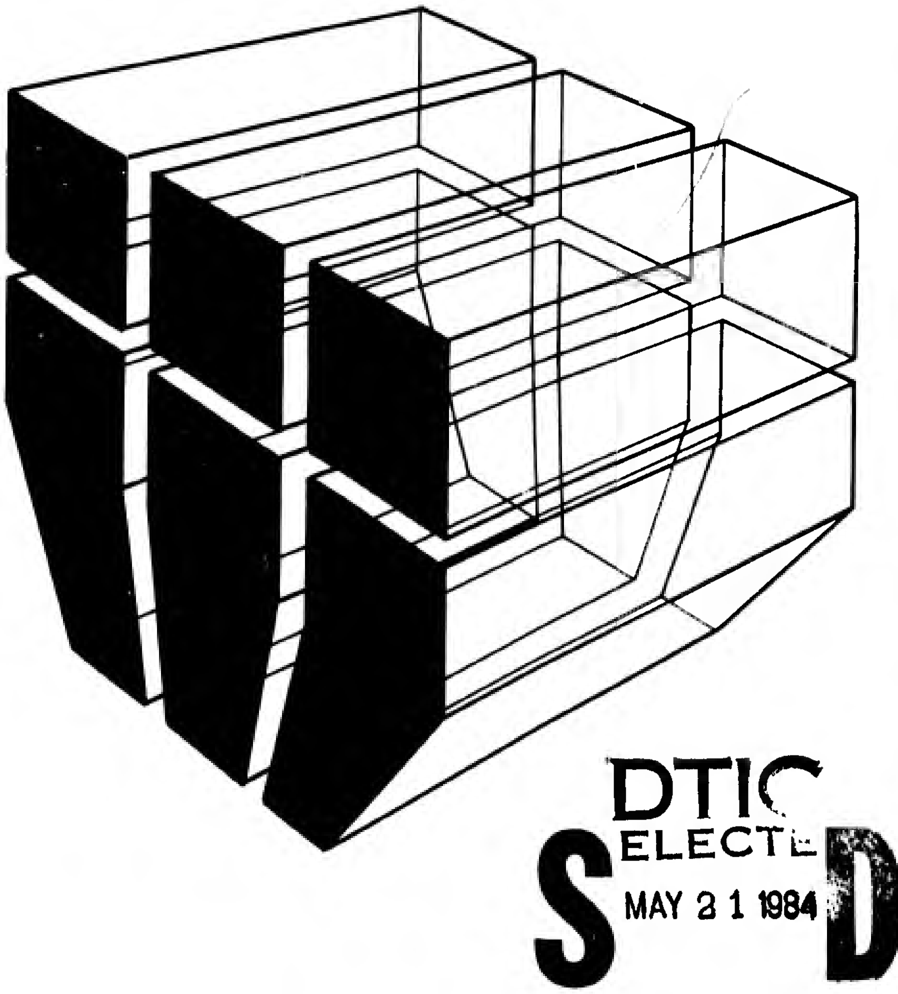

REPORT DOCUMENTATION PAGE

READ INSTRUCTIONS
BEFORE COMPLETING FORM

1. REPORT NUMBER
CERL-TR-M-345

2. GOVT ACCESSION NO.
AD-A141265

3. RECIPIENT'S CATALOG NUMBER

4. TITLE (and Subtitle)
AN INVESTIGATION INTO POLYMER DESIGN AND
SYNTHESIS FOR INFRARED ENERGY ABSORPTION

5. TYPE OF REPORT & PERIOD COVERED
Final

6. PERFORMING ORG. REPORT NUMBER

7. AUTHOR(s)
Alvin Smith

8. CONTRACT OR GRANT NUMBER(s)

9. PERFORMING ORGANIZATION NAME AND ADDRESS
U.S. ARMY
CONSTRUCTION ENGINEERING RESEARCH LABORATORY
P.O. BOX 4005, CHAMPAIGN, IL 61820

10. PROGRAM ELEMENT, PROJECT, TASK AREA & WORK UNIT NUMBERS
6.11.01A, 4A161101A91D-
04-088

11. CONTROLLING OFFICE NAME AND ADDRESS

12. REPORT DATE
May 1984

13. NUMBER OF PAGES
81

14. MONITORING AGENCY NAME & ADDRESS (if different from Controlling Office)

15. SECURITY CLASS. (of this report)
Unclassified

15a. DECLASSIFICATION/DOWNGRADING SCHEDULE

16. DISTRIBUTION STATEMENT (of this Report)

Approved for public release; distribution unlimited.

17. DISTRIBUTION STATEMENT (of the abstract entered in Block 20, if different from Report)

18. SUPPLEMENTARY NOTES

Copies are available from the National Technical Information Service
Springfield, VA 22161

19. KEY WORDS (Continue on reverse side if necessary and identify by block number)
infrared radiation
polymers
foam
energy absorbers

20. ABSTRACT (Continue on reverse side if necessary and identify by block number)

Design and synthesis of a polymer to selectively absorb infrared energy was studied. A polymer was designed that could be synthesized to incorporate a large number of different polymer groups known to absorb at the desired wavelength bands. Both film and foam specimens were prepared from the polymer, and their absorption spectra confirmed the adequacy of the design. The foamed material appeared more efficient as a masking filter for infrared of relatively short wavelength, and it is postulated that the increase is due, at least in part, to scattering by cell walls.

DD FORM 1 JAN 73 1473 EDITION OF 1 NOV 65 IS OBSOLETE

FOREWORD

This research was conducted as an In-Laboratory Independent Research (ILIR) study with joint participation between the U.S. Army Construction Engineering Research Laboratory (USA-CERL) and the Mobility Equipment Research and Development Command (MERADCOM). Funds were provided by Program 6.11.01A, "Basic Research"; Project 4A16110A91D, "In-house Laboratory Independent Research"; Task 04; Work Unit 088, "Polymer Foams as Infrared Attenuators." Mr. Alvin Smith was the USA-CERL Principal Investigator, and Dr. Jack Bond was the MERADCOM Principal Investigator.

The work was performed by CERL's Engineering and Materials Division (EM) and MERADCOM's Counter Surveillance/Counter Intrusion (CS/CI) Laboratory. Dr. Robert Quattrone is Chief of EM, and S. A. Kilpatrick is Chief of Night Vision/Camouflage at MERADCOM.

The appendix is a test report prepared by Photon Research Associates, Inc., under Contract DAAK70-79-C-0098 to MERADCOM (PRA Report No. F-019-82).

The author is grateful for the financial support of the Army's In-Laboratory Independent Research Program; to Prof. R. P. Wool of the University of Illinois at Urbana-Champaign for helpful guidance and suggestions; and to Messrs. R. G. Lampo and O. S. Marshall, co-workers who greatly assisted in the study.

COL Paul J. Theuer is Commander and Director of CERL, and Dr. L. R. Shaffer is Technical Director. COL T. Vander Els was Commander of MERADCOM.

CONTENTS

TABLES

FIGURES

FIGURES (Cont'd)

AN INVESTIGATION INTO POLYMER DESIGN AND SYNTHESIS FOR INFRARED ENERGY ABSORPTION

1 INTRODUCTION

Background

Infrared-absorption spectroscopy is used extensively in polymer chemistry in the study of reaction processes, structure, morphology, qualitative and quantitative composition, molecular configuration, and other features. The rapid growth of the technique since the mid-1940s attests to its usefulness.

This method is based on the principle that electromagnetic radiation in the infrared region (greater than λ = 0.7 m wavelength) interacts with mass in vibrational and rotational modes. The interactions with molecules or groups of atoms within molecule cause transitions between the vibrational and/or rotational states with a resulting characteristic absorption of energy or spectral "signature." The spectrum produced relates the intensity of energy absorption by specific groups of atoms at particular wavelengths. It thus provides insight into a material's composition because both the types of atoms present and their concentrations can be determined by comparing the spectrum to known absorption patterns. Infrared-absorption spectroscopy may be used alone as an analytical method; however, it is often combined with Raman and mass spectroscopy or with nuclear magnetic resonance to obtain more detailed information.

Polymers potentially can be synthesized for selective energy absorption. Such a method could lead to the development of filters for masking or altering the signatures of infrared emitting objects and, in effect, camouflage these objects against observation by attenuating or altering the infrared energy transmitted to a detector. Moreover, by foaming these polymers, filter enclosures for infrared emitters could be essentially self-supporting. The most obvious uses of selectively absorbing infrared filters are in military camouflaging applications and as photographic filters analogous to the visible light filters commonly used.

Objective

This study's objectives were to synthesize polymers to absorb energy in selective bands of the infrared spectrum and to study the effects of foaming on that polymer's overall attenuation efficiency.

Approach

A study was conducted on the mechanisms of infrared energy absorption by organic molecules, especially polymeric materials. A catalog of absorption frequencies peculiar to common polymer chemical bonds and chemical groups was compiled. Infrared spectra were made of various polymers and a polymer family capable of containing a wide variety of chemical bond types and groups was selected as a model. Solid films and foam specimens of this polymer were made and the effects of physical form and equivalent material thicknesses were judged by infrared spectra with a laboratory infrared spectrometer.

A field environment test was conducted on a selected material used as a partially enclosing filter for an electrical generating set (see Appendix). Its infrared absorption was compared to an open (unenclosed) generator over a full solar day.

Scope

This study was limited to investigating the fundamental mechanisms of infrared absorption by polymers and evaluating the effect of absorption on the polymer's physical form. A limited comparative field environment test was conducted to judge the potential for developing field-applicable infrared filters or screens to prevent or reduce observation by infrared detectors.

2 THEORETICAL

Infrared radiation energy causes only the vibrational and rotational energy state transitions described earlier; it is incapable of changing electron energy level. The transitions effected cause molecules to react as a vibrating system of springs and masses that can be reasonably approximated as a simple harmonic system. This model can be analyzed by quantum mechanics techniques such as the Schrodinger wave equation with the condition:

$$\upsilon = \frac{E2 - E1}{hc}$$

in which υ is the wave number,* E_1 and E_2 are discrete energy values of the two transition states, h is Planck's constant, and c is the velocity of light. Only vibrations causing changes in dipole moments cause infrared absorptions of a fundamental nature; overtone and combination vibrations may occur, but their intensities are generally much lower. The absorption intensity is proportional to the square of the magnitude of the changing dipole moment in the vibration or rotation.

The number of possible vibrations in a polymer system containing N atoms is 3N wave numbers. Of these, six values represent whole molecule vibrational or rotational transitions, so the total number of possible absorptions becomes 3N-6 in most cases. Not all vibrations are detectable in the infrared spectrum due to a lack of proper response by the molecule or group to the infrared energy or to precedent Raman (electrical polarizability) activity or molecular symmetry. It is possible to calculate values for all vibration frequencies from atomic masses and geometric positions (chemical bond lengths and bond angles). Force constants of the bonds can also be determined if some of the values are provided independently from other sources such as mass spectroscopy and nuclear magnetic resonance.

The translations of vibrational or rotational energy via mass displacement occur as bond stretching (symmetric and asymmetric), deformation (symmetric bending), wagging, twisting, and rocking as defined and illustrated by Bikales.[1] In relatively simple polymer molecules such as polyethylene, the motions are well defined. More complex molecules, especially network or crosslinked polymers with a great number of different group types, present much more formidable problems of exact analytical description. Nearest neighbor interactions, hydrogen bonding, van der Waals forces, residual strain, and steric hindrances all may cause shifting of the absorption band in the spectrum, broadening of the band, or combination with other nearby bands, concomitantly altering the absorption intensity.

The amount of infrared energy absorbed (converse of transmitted) as an infrared beam is passed through a material depends linearly on the incident radiation intensity and nonlinearly on the number of absorbing molecules or groups in the path. The functional relationship is given by the Beer-Lambert

---

*The wave number is conventionally defined as 104/λ, where λ is between 1 and 500 m; it allows better numerical description than does wavelength.

[1] N. M. Bikales, Characterization of Polymers (Interscience, 1971), pp 127-129, 133.

law,[2] in which logarithms are required to give the correct quantitative value of absorption. Since the effect of the logarithm is less pronounced with weak absorption, the difference in peak absorption can be used to describe the number of absorbing molecules or groups. The reverse is not true, however, since strong absorption results in very large changes in the logarithmic value of transmission, and care must be exercised in interpreting the results quantitatively with respect to the number of functional absorbing groups in the light path.

Given that each polymer group has characteristic absorption properties, it is theoretically possible to select groups by type and quantity and to synthesize polymers that absorb at specific bands in the spectrum. As a result, infrared radiation incident on one side of a layer of such a material can be absorbed as it passes through with the shape and/or overall transmitted spectrum intensity tailored to suit a desired result.

Relatively little work has been reported on the intentional design of polymers to absorb infrared energy over a substantial portion of the near and intermediate portions of the spectrum. Exceptions include long- and short-pass and interference filters designed principally for use in studying the infrared spectrum itself.[3]

---

[2] J. F. Rabek, Experimental Methods in Polymer Chemistry (Interscience, 1980), pp 212, 224.

[3] W. L. Wolfe and G. J. Zissis (eds.), The Infrared Handbook (Office of Naval Research, Department of the Navy, 1978), pp 7-110.

3 EXPERIMENTAL

The experiment proceeded as follows: First, a polymer system was chosen to afford as much flexibility in molecular design as practical. Second, the designed polymer was synthesized. Third, the infrared-absorption spectrum of the polymer was studied with the polymer as a film and as varying thicknesses of foam to determine whether that polymer absorbed as designed and to compare film and foam performance.

Polymer groups were cataloged with respect to their infrared absorption bands. The selected groups and references are given in Table 1. The groups with their vibrational modes and principal absorption bands are listed in Table 2. These tables do not cover the entire range of possibilities, but rather reflect a selection broad enough to cover a reasonable portion of the infrared spectrum from wave number 4000 cm^{-1} to about wave number 700 cm^{-1}. More than 100,000 infrared spectra are available for comparison reference of polymer group absorption in the ASTM and Sadtler collections.[4] To design a polymer molecule to enhance absorption at a particular wavelength, a group or groups with strong absorption at the desired frequency can be selected from Table 2 and the molecule can be made to have an abundance of these groups.

An examination of numerous polymer compositions showed that the polyurethane family offered potential for including many of the desired groups. (For contrast, polyethylene contains only CH_2 groups with no possibility of adding groups other than CH_3 at the chain ends.) Furthermore, the polyurethanes in general readily synthesized as both films and foams by using commercial isocyanates and a wide variety of reactants that contain ether (C-0), ester (-C(=0)-0), phosphate (PO_4^{-3}), amine (NH), amide (-C(=0)-NH_2), sulfur (S-H), halogen (C-X), silicon (Si-H, Si-C, Si-0), and other groups. Figure 1 depicts the general absorption assignments of the various groups, which cover the entire spectrum from about 3600 cm^{-1} to 700 cm^{-1} wave numbers.

The polyurethane was formulated using a polymethylenepolyphenylisocyanate and a polyether polyol. The chemistry and reactions are described elsewhere,[5] and the general chemical structure is shown in Figure 2. Thin films of the formulated polyurethane were cast on a Teflon slab. Low-density foams were made of the same formulation but, by necessity, the foams also contained silicone surfactant and monofluorotrichloromethane as a cell control and foaming agent, respectively. The foam was sliced into thin sheets of various thicknesses prior to testing.

Transmission spectra of the specimens were made on a Perkin-Elmer Infrared Spectrometer, Model 283B. The transmission method was selected over other techniques such as attenuated total reflectance or as particles dispersed and consolidated in potassium bromide pellets as described by Bikales.[6] The transmission mode represents the anticipated use as a filter and was thus

---

[4] J. F. Rabek.

[5] J. H. Saunders and K. C. Frisch, Polyurethanes, Chemistry and Technology-Part 1 Chemistry (John Wiley & Sons, 1962).

[6] N. M. Bikales.

Table 1

Groups of Interest and Applicable References

Group	References
-CH	Bellamy (1975); Dolphon & Wick (1977); Colthup, et al. (1964); Whetsel (1969); Potts & Nyquist (1959); Pinchas (1955); Katritzky (1959).
CH_2	Bellamy (1975); Colthup, et al. (1964); Dolphin & Wick (1977); Whetsel (1969); Fox & Martin (1940); Francis (1951); Wright (1959); McMurry & Thorton (1952); Jones (1957); Sheppard (1959); Potts & Nyquist (1959); Davison & Bates (1953).
CH_3	Bellamy (1975); Colthup, et al. (1964); Dolphin & Wick (1977); Szymanski (1964); Whetsel (1969); Fox & Martin (1940); McKean (1971); Francis (1951); Wilmshurst (1957).
C-X (X=halogen)	Bellamy (1975); Altona & Hageman (1969); Rently, et al. (1964).
C-C	Bellamy (1975); Simpson & Sutherland (1949).
$\dot{C}=\dot{C}$ (aromatic)	Bellamy (1975); Colthup, et al. (1964); Dolphin & Wick (1977); Varsanyi (1969).
C=C	Bellamy (1979); Colthup, et al. (1964).
$C\approx C$	Bellamy (1979); Colthup, et al. (1964); Hummel (1974); Matsubara, et al. (1966).
C=N	Bellamy (1975).
$N\tilde{H}$	Bellamy (1975); Colthup, et al. (1964); Dolphin & Wick (1977); Hummel (1974); Bellamy (1968); Whetsel (1969); Murthy & Rao (1969).
NH_2	Bellamy (1975); Colthup, et al. (1964); Dolphin & Wick (1977); Whetsel (1969); Stewart (1959); Flett (1963).
C-O	Bellamy (1975); Colthup, et al. (1964); Hummel (1974) Stuart & Sutherland (1956).
C=O	Bellamy (1975); Colthup, et al. (1964); Dolphin & Wick (1977); Hummel (1974); Bellamy (1968).
OH	Colthup, et al. (1964); Dolphin & Wick (1977).
P-H	Colthup, et al. (1964); Daasch & Smith (1951).
PO_4^{-3}	Colthup, et al. (1964).

Table 1 (Cont'd)

Group	References
P=O	Bellamy (1975); Daasch & Smith (1951).
Si-H	Colthup, et al. (1964); Kniseley, et al. (1959).
Si-O	Colthup, et al. (1964); Wright & Hunter (1947); Smith (1960).
Si-C	Colthup, et al. (1964); Smith (1960).
Si-X	Colthup, et al. (1964); Smith (1960).
SO_4^{-2}	Colthup, et al. (1964).
C-S	Colthup, et al. (1964); Sheppard (1950).
ONO_2, NO_3^{-1}	Bellamy (1975); Colthup, et al. (1964); Carrington (1960).

Table 2

Tabulation of Groups with Principal Vibrational Modes and Absorption Bands

Group	Association	Stretching, cm^{-1}	Deformation, cm^{-1}	Wagging, cm^{-1}
C-H	Aliphatic	2880-2900 (w)	1315-1350 (w)	
	Aromatic	3030 (w m)	700-900 (s) out-of-plane 100-1300 (m) in-plane	
	Alkynes	3267-3340 (s)	610-680 (s)	
	Alkenes	3000-3030 (m)	trans 965 990 (s) out-of-plane cis 650 730 (m) trans 1285-1300 (m) in-plane cis 1395-1430 (m) in-plane	
	Halogen carbons	3000	1200-1215 intensifies	
	Carbonyl esters	2900-2930	1400	
	Amides			
CH_2		2916-2936 (s) asym 2843-2063 (m) sym	1450-1475 (m)	
CH_3	Aliphatic	2952-2972 (s) asym 2862-2882 (m) sym	1450-1475 (m) asym 1370-1380 (m) sym	
	Aromatics	2920-2930 (m) asym 2860-2870 (m) sym		
C-F		1000-1400 (vs)		
C-Cl		650-730 (m to s)		
C-Br		510-700		
C-I		485-600		
C-C		1140-1250 (s)		
$\dot{C}$-$\dot{C}$	1440-1625 (w m)		Ring stretching	

Table 2 (Cont'd)

Group	Association	Stretching, cm^{-1}	Deformation, cm^{-1}	Wagging, cm^{-1}
$C{=}C$		1638-1692 (w m)		
$C{\equiv}C$		2100-2260 (m w), depending on substitution		
C-N	Amines, aliphatic	1032-1090 (m) asym		
	aromatic	1250-1360 (s) asym		
	Guide primary	1310-1430 (w)		
	secondary	1270 (s) as Amide III		
			1515-1570 (s)	
$C{\equiv}N$	Alkyl	2240-2260 (s)		
	Aryl	2220-2240 (s)		
N-H	Secondary amines	3310-3360 (w)	1550-1650 (w)	700-750 (m)
	Secondary amines	3140-3480 (m)	1200-1305 (m) Amine III	700-740 (m)
	Urethanes	3250-3340 (m)	1200-1305 (m)	700-740 (m)
NH^2	Amines	3330-3400 (w)	1575-1660 (m)	750-350 (s)
	Amides	3350 (m)	1620-1650 (s)	600-750 (s)
C-O	Ethers, alkyl	1060-1150 (vs)		
	aromatic	1230-1270 (vs)		
	alkyl/aryl	1010 1050 (s)		
	vinyl	1200-1225 (s)		
	Esters	1160-1210 (s)		
	Acetate	1230-1260 (s) asym		
		1035-1060 (s) asym		
	Carbonates, alkyl/alkyl	1240-1280		
	alkyl/aryl	1211-1248		
	aryl/aryl	1205-1221		

Table 2 (Cont'd)

Group	Association	Stretching, cm^{-1}	Deformation, cm^{-1}	Wagging, cm^{-1}
C=0	Amides, ureas, urethanes, carbon acids, carbonates, etc.	1600-1700 (s)		600-700
OH	Alcohols Carboxy acids Phenols	3300 (s) 3000 (s) 3200-3250	1260-1350 (s) 875-960 (m) 1211-1320 (s) 1180-1260 (s)	1260-1350 (s)
P-H		2275-2320 (m)	1080-1090 (m)	910-940 (m)
PO_4^{-3}	1000-1100 (s)			
P=0		1110-1250		
Si-H		2100-2250 (m)	800-950 (m)	800-845 (m)
Si-0	Siloxanes (open-chain) Alkoxy Silanols	1024-1055 (s) 1076-1095 (s) 1100 (m) 830-910 (s)		
Si-C	Methyl siloxanes Si-phenyl	660-850 (m) 1100-1125 (s)		
Si-X	(X = Halogen)	820-945 (s)		
SO_4^{-2}	1080-1125 (s) asym			

Table 2 (Cont'd)

Group	Association	Stretching, cm^{-1}	Deformation, cm^{-1}	Wagging, cm^{-1}
C-S	Aliphatic	570-705 (m w)		
	Aromatic	1090		
ONO_2		1270-1285 (9s) Sym	745-760 (m) 690-710 (m)	
NO_3^{-1}	1350-1380 (s)			
		815-835 (m)		

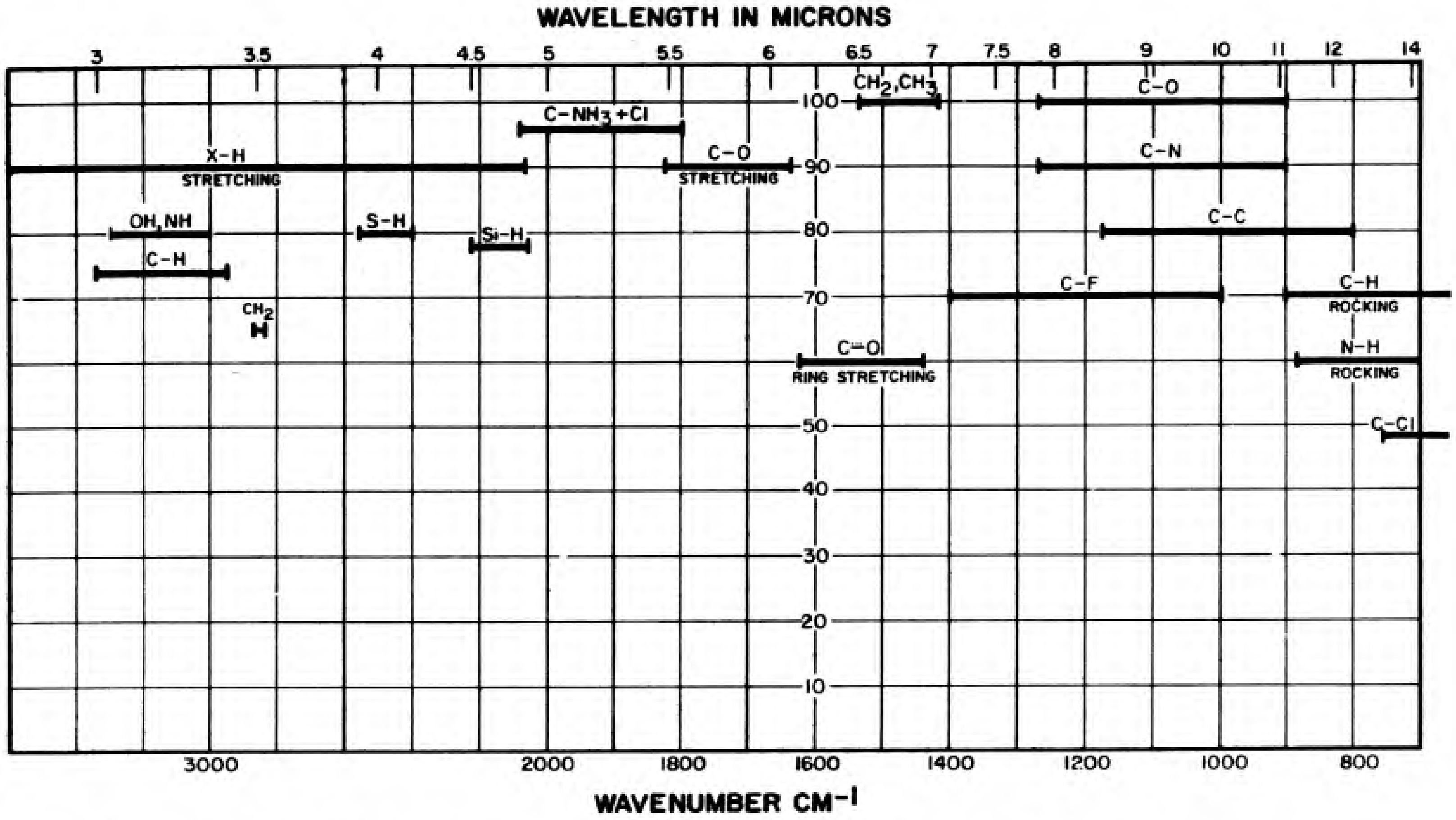

Figure 1. General description of the absorption bands of some polymer groups.

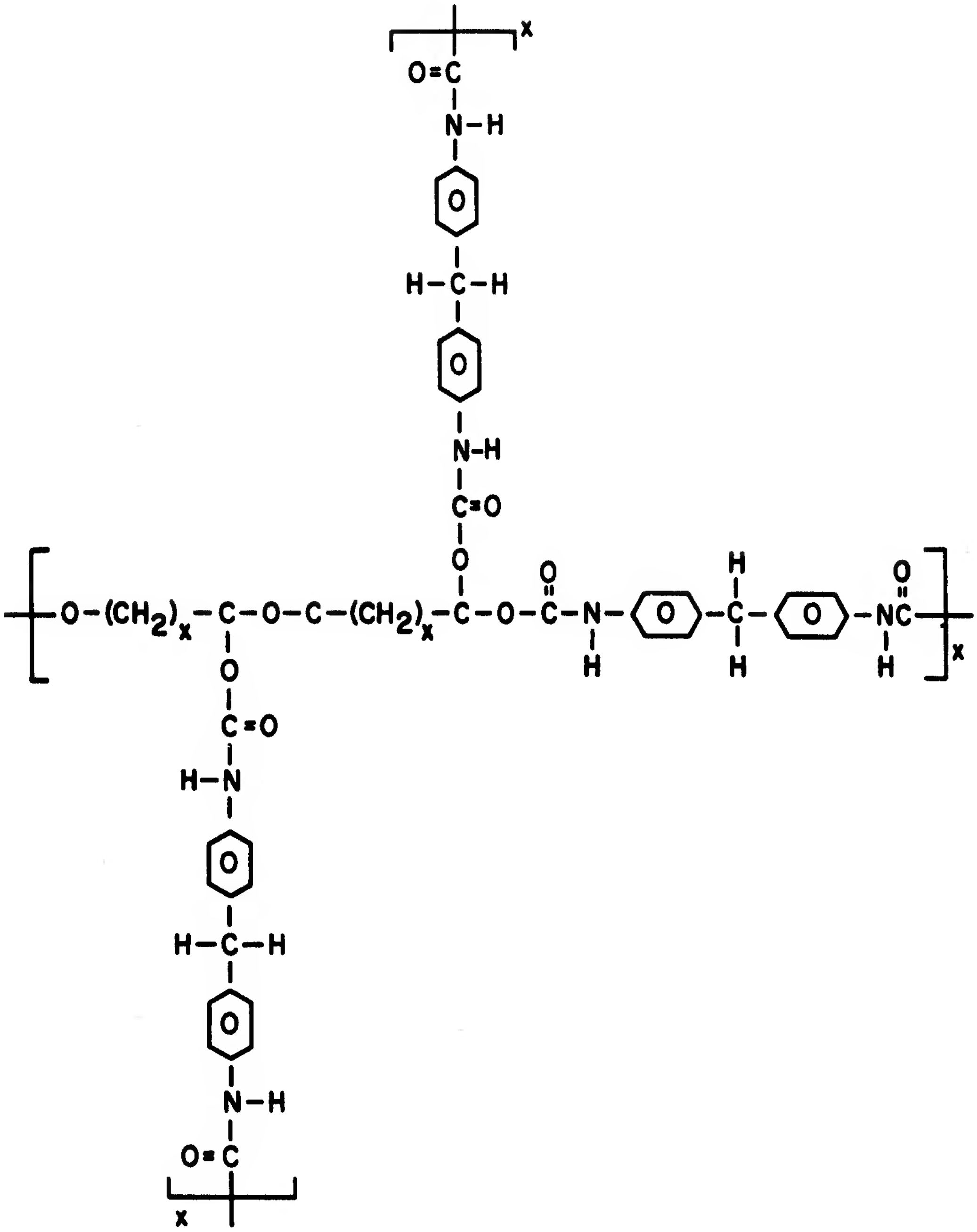

TYPICAL ...... STRUCTURE

Figure 2. Typical structure of a polymethylene polyphenylisocyanate/ polyether polyol polyurethane polymer.

considered the most appropriate test procedure. Comparable absorption spectra were obtained for the film and foam specimens; thus, the method appeared satisfactory.

4 RESULTS AND DISCUSSION

A composite spectrograph of the film and foam specimens is shown as Figure 1. Curve 1 at the top of the graph is the transmission spectrum of a thin film (0.0178 mm) of the polyurethane polymer. Absorption peaks (which appear as valleys in the curve) are strong at numerous wave numbers, especially at about 1075 cm^{-1}, 1220 cm^{-1}, 1525 cm^{-1}, 1710 cm^{-1}, 2900 cm^{-1}, and 3300 cm^{-1}. The presumed absorbing groups are identified in the upper margin. Curves 2 through 5 are increasingly greater thicknesses of foam (0.0218 mm through 0.0533 mm) of the same polymer and, as can be seen, they retain the same general absorption features as the film; however, the absorption peaks become less pronounced as the thickness increases and more total absorption occurs. A sufficiently thick specimen would totally block transmission and the whole spectrum would be absent, just as though no specimen in the beam would allow complete transmission.

The somewhat erratic trace of the curves is probably due to reflective scattering of the beam; small deviations in the curve are not satisfactory for assignment of absorption groups. Nor should these small peaks be considered indicative of the dipole activity required for infrared absorption. Instead, they should be considered artifacts of the test or ignored completely for the purposes of this study.

The multiple absorption peaks shown in Figure 3 result from the variety of different groups present in the polyurethane polymer. In addition to the prominent peaks described, many smaller peaks are evident. The overall absorption spectrum is essentially the form desired and could effectively filter an emission spectrum from an infrared source.

The foam specimens absorbed more than the equivalent solid film as shown in Table 3. The increased absorption is attributed to substantial scattering caused by the large number of angles described by cell walls in the foam. Incidence of the beam with the cell walls at various angles increases reflection sideways and backward.

The results of this study support the hypothesis that selectively absorbent polymers can be designed and synthesized. Foamed polymer appears to be superior to a film of the same material with thickness when used as a filter for infrared radiation. It is believed that effective masking filters for emitters could be made to a particular specification for absorbing much of the infrared spectrum within the range described in this paper.

Although not included in this study, it is known that colorants, dyes, pigments, and fillers can also be incorporated into a polymer (film or foam) to further alter the absorption properties.

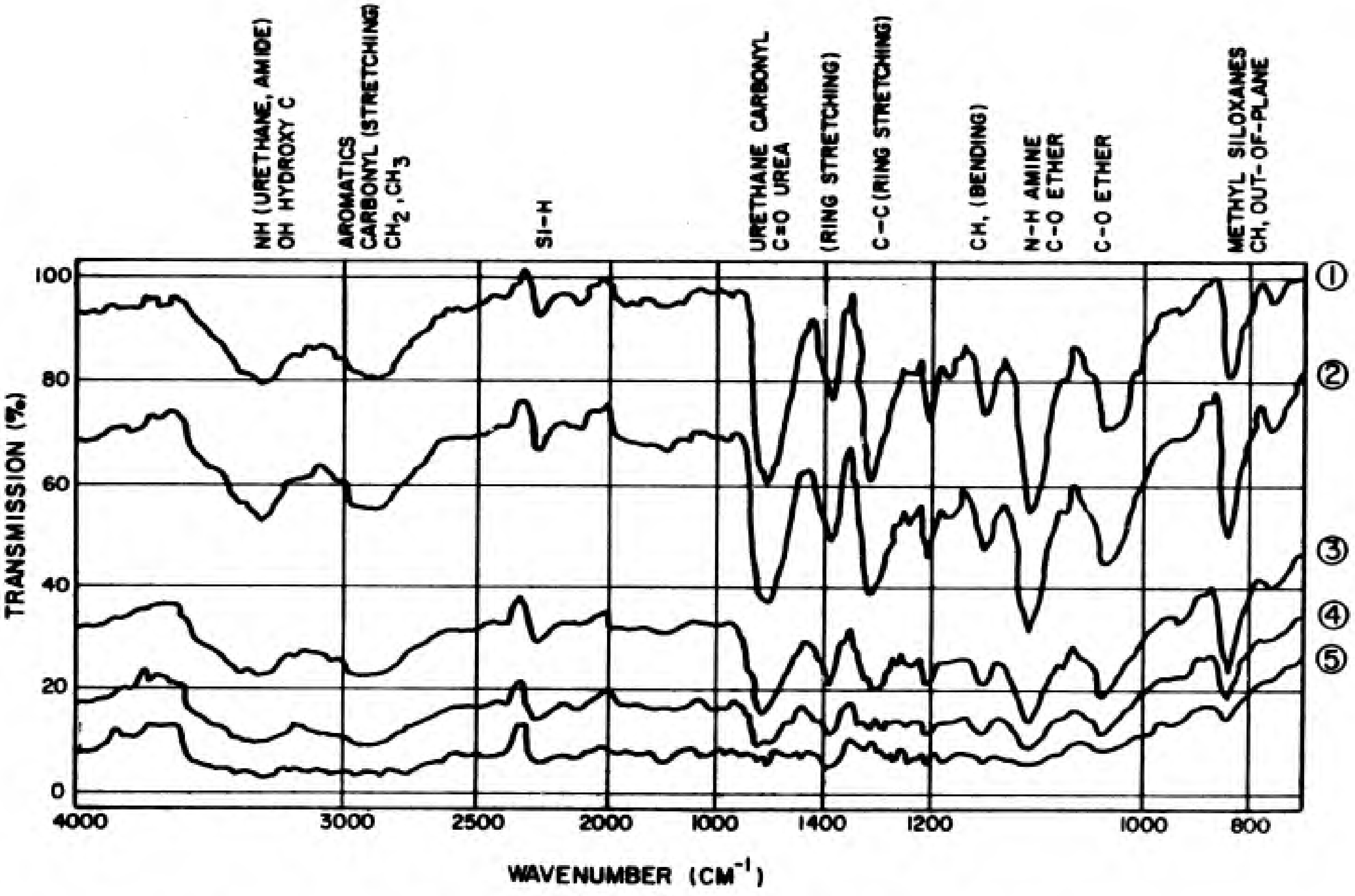

Figure 3. Comparison of polyurethane film and foam absorption spectra.

Table 3

Equivalent Solid Film/Foam Thickness and Relative Absorption at 3000 cm^{-1}

Foam Thickness, mm	Film Thickness Equivalent, mm	% Absorption
0.61	0.0178*	16.5*
0.76	0.0218	40
1.04	0.0305	75
1.50	0.0432	90
1.91	0.0533*	96*

*It is readily apparent that a three-fold increase in equivalent thickness causes almost a six-fold increase in absorption at this wave number. Essentially, the same ratio occurs all along the spectrum of 4000 cm^{-1} to 700 cm^{-1}.

5 CONCLUSIONS AND RECOMMENDATIONS

Polymers can be selected or new types designed that absorb infrared energy in the near and intermediate regions (4000 to 700 cm^{-1}). Chemical bonds and groups have unique absorption frequencies; therefore, selection or design of a polymer with an abundance of specific groups can effectively filter absorption. Similarly, wide band absorption can be afforded by including a variety of different bonds and/or groups in the polymer.

Foamed polymers are more efficient filters on an equivalent material basis.

Foamed poyurethane polymer can be used to filter infrared energy emitted by a source such as an electrical power generator. Specific design features must exist in the foam enclosure to avoid negative contrasts with background radiation and to eliminate emissivity lags with solar heating and cooling cycles.

It is recommended that the effects of thermal source temperature, filter stand-off distance (air gap) from the source, and foam filter thickness be further studied in terms of their interdependence or interrelationships. Information gained may provide design criteria for filter systems to be used as infrared camouflage.

If design criteria become established, it is further recommended that material systems for infrared camouflaging of selected thermal sources on the battlefield be developed.

CITED REFERENCES

Altona and Hageman, Rec. Trav. Chim. Pays Bas, Vol 88 (1969), p 33.

Bellamy, L. J., Advances in Infrared Group Frequencies (Methuen & Co., 1968).

Bellamy, L. J., The Infrared Spectra of Complex Molecules, 3rd Ed. (Chapman and Hall, 1975).

Bikales, N. M., Characterization of Polymers (Interscience, 1971), pp 127-129, 133.

Carrington, R. A. G., Spectrochim. Acta., Vol 16 (1960), p 1279.

Colthup, N. B., L. H. Daly, and S. E. Wiberley, Introduction to Infrared and Raman Spectroscopy (Academic Press, 1964).

Daasch, L. W., and D. C. Smith, Anal. Chem., Vol 23 (1951), p 853.

Davison, W. H. T., and J. Bates, Chem. Soc. (1953), p 2607.

Dolphin, D., and A. Wick, Tabulation of Infrared Spectral Data (Wiley-Interscience, 1977).

Flett, M. S. C., Spetrochim. Acta., Vol 19 (1963), p 509.

Fox, J. J., and A. E. Martin, Proc. Royal Soc., Vol A175 (1940), pp 208, 234.

Francis, S. A., J. Chem. Phys., Vol 19 (1951), p 942.

Hummel, D. O., Applied Infrared Spectroscopy, Chapt 2.2 in D. O. Hummel (ed.), Polymer Spectroscopy, Monographs in Modern Chemistry, Vol 6 (Verlag Chemie, 1974).

Jones, R. N., Spectrochim. Acta., Vol 9 (1957), 235.

Katritzky, A. R., Quart. Rev., Vol 13 (1959), p 353.

Kniseley, R. N., V. A. Fassel, and E. E. Conrad, Spectrochim. Acta., Vol 15 (1959), p 651.

Matsubara, I., Y. Itch, and M. Shinomiya, J. Polymer Sci., Vol B4 (1966), p 47.

McKean, D. C., Chem. Comm. (1971), p 1373.

McMurry, H. L., and V. Thorton, Anal. Chem., Vol 24 (1952), p 2318.

Murthy, A. S. N., and C. N. R. Rao, "Spectroscopic Studies of the Hydrogen Bond," Appl. Spectros. Rev., Vol 2 (1969), p 69.

Pinchas, S., Anal. Chem., Vol 27 (1955), p 2.

Potts, W. J., and R. A. Nyquist, Spectrochim. Acta., Vol 15 (1959), p 679.

Rabek, J. F., Experimental Methods in Polymer Chemistry (Interscience, 1980), pp 212, 224.

Rentley, F. F., N. T. McDevitt, and A. L. Rozek, Spectrochim. Acta., Vol 20 (1964), p 105.

Saunders, J. H., and K. C. Frisch, Polyurethanes, Chemistry and Technology--Part 1 Chemistry (John Wiley and Sons, 1962).

Sheppard, D., Trans. Faraday Soc., Vol 46 (1950), p 429.

Sheppard, N., Advances in Spectroscopy, Vol 1 (Interscience (1959), p 288.

Simpson, D. M., and G. B. B. M. Sutherland, Proc. Royal Soc., Vol A199 (1949), p 169.

Smith, A. L., Spectrochim. Acta., Vol 16 (1960), p 87.

Stewart, J. E., J. Chem. Phys., Vol 30 (1959), p 1259.

Stuart, A. V., and G. B. B. M. Sutherland, J. Chem. Phys., Vol 24 (1956), p 559.

Szymanski, H. A., IR: Theory and Practice of Infrared Spectroscopy (Plenum Press, 1964).

Varsanyi, G., Vibrational Spectra of Benzene Derivatives (Academic Press, 1969).

Whetsel, K. B., "Near Infrared Spectrophotometry," Appl. Spectros. Rev., Vol 2 (1969), p 1.

Wilmshurst, J. K., J. Chem. Phys., Vol 26 (1957), p 426.

Wolfe, W. L., and G. J. Zissis (eds.), The Infrared Handbook (Office of Naval Research, Department of the Navy, 1978), pp 7-110.

Wright, N., and M. J. Hunter, J. Am. Chem. Soc., Vol 69 (1947), p 803.

Wright, W. B., J. Org. Chem., Vol 24 (1959), p 1362.

UNCITED REFERENCES

Hummel, D. O., "Infrared Spectra of Polymers," Polymer Reviews, Vol 14 (Wiley-Interscience, 1966).

Hummel, D. O., and F. Scholl, Infrared Analysis of Polymers, Resins, and Additives: An Atlas, Vol 1, Part 2 (Wiley-Interscience, 1969).

Krimm, S., "Infrared Spectra of High Polymers," Fortschr. Hochpoly.-Forsch., Vol 2 (1960), p 51.

Mason, P., J. Chem. Soc. (1961), p 22.

Szymanski, H. A., and R. E. Erickson, Infrared Band Handbook, 2nd Ed. (IFI/Plenum, 1970).

Tadokoro, H., and M. Kobayashi, "Vibrational Analysis of Highly Ordered Polymers," Chapt 2.2, D. O. Hummel (ed.), Polymer Spectroscopy, Monographs in Modern Chemistry, Vol 6 (Verlag Chemie, 1974).

Zbinden, R., Infrared Spectroscopy of High Polymers (Academic Press, 1964).

APPENDIX:

INFRARED ABSORPTION BY POLYMERS--EVALUATION OF A CAMOUFLAGE CONCEPT

1 TECHNICAL APPROACH

The performance of the camouflage material (Figure A1) was evaluated in a field experiment in which two 60-kW diesel generators were deployed at Fort Sill, Oklahoma. One generator was covered with a shell of the foam sheets supported on a wood frame. The second was used as a control, operated under similar conditions as the first but lacking the shell.

The fundamental question underlying the experiment was whether the foam material would be useful as an infrared camouflage. The baseline for the test was established as the 60-kW diesel generator with a generator exhaust suppression system (GESS). This combination was used because neither side shields nor exhaust area suppression devices alone can alleviate the thermal threat.

Temperature and environmental data were recorded for a full 24-hr period to provide an accurate description of the foam's performance under a variety of conditions. The data were used to produce infrared thermal models of the camouflaged and uncamouflaged generators. These thermal models were then used to predict the target signature contrast and detectability as a function of range, azimuth, elevation, time of day, and background type for the suppressed and unsuppressed targets.

Validation of the target detectability was planned. Unfortunately, the overflights were canceled; it would have been advantageous to check the quantitative aspects of the detection model. However, the differences between the suppressed and unsuppressed targets were so qualitatively clear-cut that the assessment of the camouflage material's worth did not suffer.

The value of the polyurethane foam sheets was assessed by measuring the degree to which the apparent temperature differentials (with respect to the apparent background temperature) of various generator surfaces were suppressed, thereby affecting the unit's detectability. As a result of this data analysis, conclusions could be reached about benefits provided by the foam. Furthermore, this exercise pointed out certain simple modifications of this material that would substantially improve its performance.

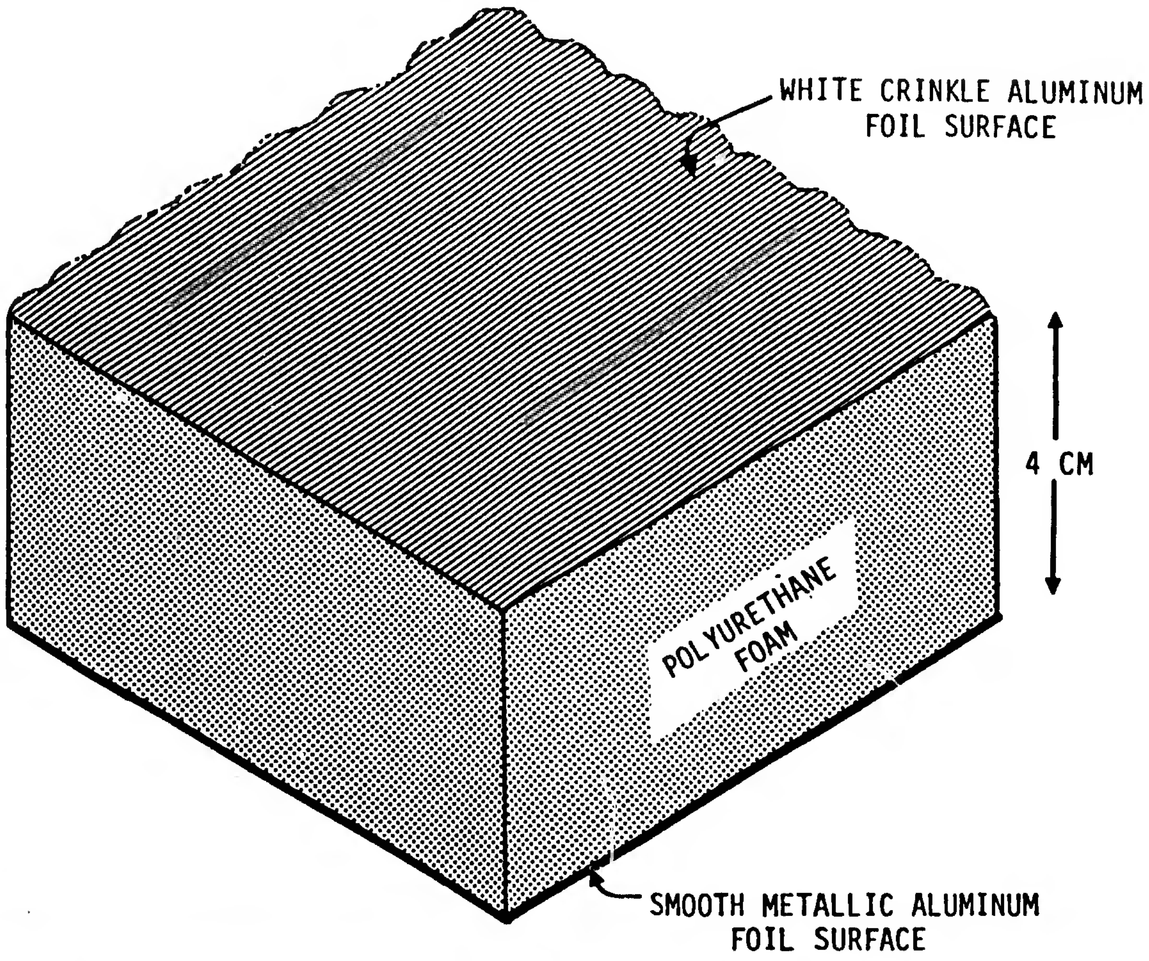

Figure A1. Schematic description of CERL candidate camouflage material.

2 PHYSICS OF THERMAL MEASUREMENTS

This experiment pointed out limitations in the ability to measure specific quantities accurately. A brief review of limitations presented by the basic physical laws and by the state of current instrumentation is presented to explain why certain procedures were followed in the data collection.

Discrepancies between temperatures measured by thermocouple and those recorded by the PRT-5 radiation thermometer can result from (1) an emissivity of the surface less than the one over the infrared radiometer's band pass, (2) a significant external infrared source that renders the radiometer's measurements incorrect, and (3) poor thermodynamic equilibrium between the surface and the contact probe. Examples of all three error sources were identified as the data were taken for this study. Of course, the affected data were corrected or discarded.

The first and second causes of measurement error affect the apparent temperature measurements made by the PRT-5 radiometer or a similar device. These radiometers do not actually measure temperature, but rather respond to infrared radiation they receive from a certain direction. The radiation received when looking along a certain line-of-sight is expressed as:

$$N_a = N_{path} + \tau_{path} * (H_i \rho + L_e(T) \cdot \varepsilon) \quad \text{[Eq A1]}$$

where N_a is the apparent radiance

N_{path} is the radiance along the path for the sensor to the target

τ_{path} is the transmission along the same path

H_i is the irradiance from the surrounding environment impinging upon the target surface

ρ is the reflectance of the target surface

$L_e(T)$ is the radiance that would be radiated by a perfectly emissive surface at a temperature T

ε is the emissivity of the surface

This equation is true only for a single wavelength and must be expanded into an integral over wavelength, with each term a function of wavelength, to correctly compute the radiation perceived over a certain wavelength interval for a given line-of-sight.

The accuracy of the PRT-5 is based on several simplifying factors that usually permit a direct measurement of surface temperature from apparent infrared radiance. This instrument uses a wavelength region of 8 to 14 microns, which provides these simplifying factors. In this region, over fairly short paths (on the order of meters or tens of meters), the path radiance, N_{path}, is negligible and the transmission, τ_{path}, is close to 1. Furthermore, the reflectivity, ρ, of many materials is negligible (conversely, the emissivity ε is nearly one). Under these conditions, Equation A1 condenses to the following much simpler form:

$$N_a = L_e(T) \qquad \text{[Eq A2]}$$

It is a simple matter to convert from the emitted radiance of the surface, $L_e(T)$, to the temperature itself, T, by Planck's law.

This concept is the general foundation for the radiation thermometer. Thus, the potential pitfalls of apparent temperature measurement should be clear. The most common problem, and one encountered in this study, is presented when the reflectivity of the surface is not negligible and the simple Equation A2 no longer is applicable. Instead,

$$N_a = \rho H_i + \varepsilon \cdot L_e(T) \qquad \text{[Eq A3]}$$

Under these conditions ($\varepsilon \neq 1$), the measurement is contaminated by radiation stemming from external sources. The degree of this contamination is directly related to the reflectance, ρ. If the external sources are colder than the target surface, the temperature will appear lower than the actual surface temperature. The opposite is true if the external sources are warmer than the target surface.* This specific problem in measurement accuracy was encountered when attempting to measure the radiative temperature of the aluminum-surfaced foam.

The third common source of discrepancy between contact and apparent measurements lies not with an inaccuracy of the apparent measurement but with that of the contact thermocouple. The contact probe operates by drawing energy from the surface being measured. Ideally, the energy required to bring the probe to the same temperature as the surface is small. Figure A2 illustrates the heat fluxes associated with this process. Between each node of the thermodynamic model is a temperature drop, ΔT:

$$\Delta T = j/h \qquad \text{[Eq A4]}$$

where j is the thermal flux

h is the thermal conductivity between the nodes.

Also:

$$\Delta T_{s-e} = \Delta T_{s-c} + \Delta T_{c-p} + \Delta T_{p-e} \qquad \text{[Eq A5]}$$

where ΔT_{s-e} is the total temperature difference between the environment and the undisturbed surface

ΔT_{s-c} is the temperature difference between the undisturbed surface and the surface in contact with the probe

ΔT_{c-p} is the temperature difference between the surface in contact with the probe and the probe itself

ΔT_{p-e} is the temperature difference between the probe and the environment.

The combination of Equations A4 and A5 show that the error in the surface temperature measurement, ΔT_{s-p}, can be expressed as:

---

*One other source of error occurs when the optical path is long and τ_{path} ceases to be unity. This situation never arose for the present study since the distance between the PRT-5 sensor and the surface being measured was always less than 1 m.

PHYSICAL MODEL SHOWING HEAT FLUXES

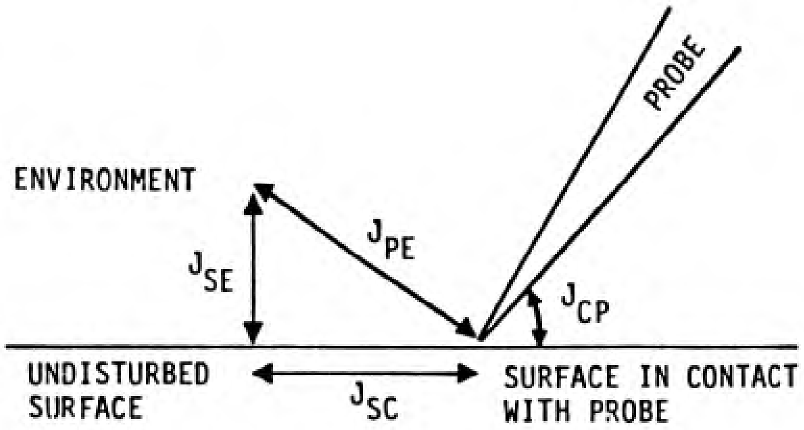

THERMAL MODEL SHOWING NODE TEMPERATURES AND THERMAL CONDUCTANCES

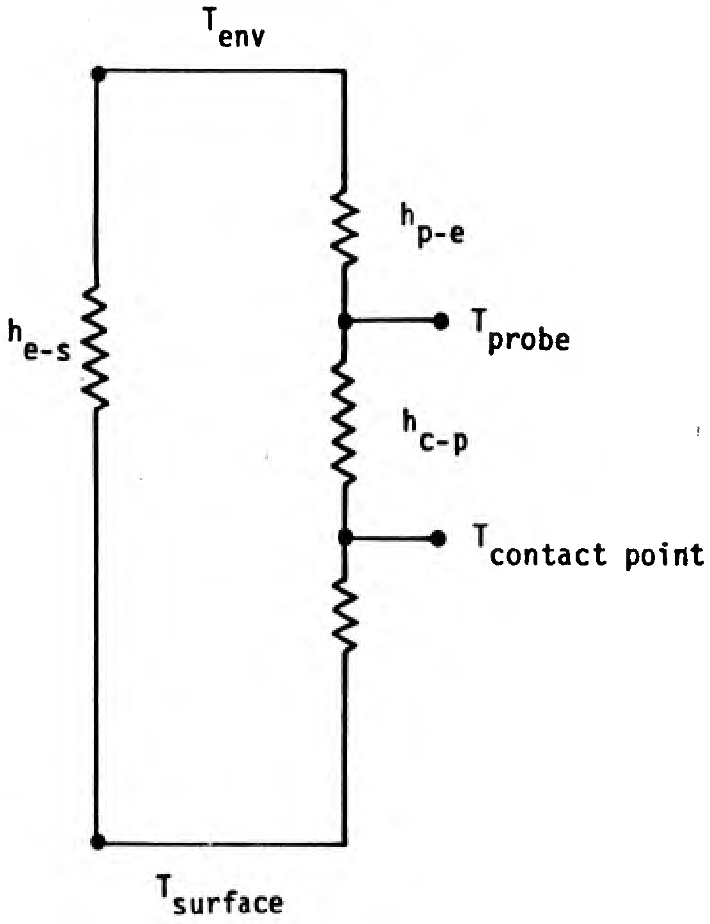

Figure A2. Heat fluxes involved in contact temperature measurement.

$$\Delta T_{s-p} = \Delta T_{s-e} * \left(\frac{\frac{1}{h_{s-c}} + \frac{1}{h_{c-p}}}{\frac{1}{h_{s-c}} + \frac{1}{h_{c-p}} + \frac{1}{h_{p-e}}} \right) \qquad \text{[Eq A6]}$$

where ΔT_{s-p} is the error in temperature measurement

h_{s-c} is the heat conductance between the undisturbed surface and that in contact with the probe

h_{c-p} is the heat conductance between the surface in contact with the probe and the probe itself

h_{p-e} is the heat conductance between the probe and the environment.

Equation A6 shows clearly when the error associated with the thermocouple reading will be significant. The error will be large if the surface temperature is significantly different from that of the environment. In addition, this error will be expressed only when the sum of $1/h_{s-c} + 1/h_{c-p}$ approaches or exceeds $1/h_{p-e}$.

There were several instances during the experiment in which contact probe temperatures were not taken due to the inability to obtain correct readings as discussed above. Particularly affected were contact measurements of the foam, either in its bare state or when surfaced with aluminum foil.

3 RESULTS

To develop an accurate description of the infrared appearance of the unsuppressed and suppressed 60-kW generators under a variety of conditions contact and apparent temperature measurements were made on the two units.

The actual field measurements began by scanning each of the two generators to identify points on the units that would suffice to represent accurately the temperature distribution. The points chosen for measurement were marked with thermal contact paste to insure the accuracy of the contact thermocouple measurements and that the measurements were always made at the same place. Figure A3 shows the points chosen to represent the temperature distribution of the uncamouflaged generator, and Table A1 contains the thermocouple and PRT-5 raw temperature data for this stock set.

More than one thermocouple often was used to make the contact measurements for one time point, and in those cases, the average of the data was used. At no time was there any significant disagreement among the thermocouple devices used, encouraging the belief that the data were accurate. Furthermore, all discrepancies between the thermocouple and PRT-5 measurements were observed to have resulted from the third (thermal flux) problem discussed in Chapter 2. These discrepancies prevailed when measuring the hot exhaust louvres. It was extremely difficult to make good thermal contact with these surfaces due to the dust and soot covering them and the thermal contact paste. Therefore, it was decided to rely on the PRT-5 measurements in these cases for a more accurate measure of the thermal distribution.

An important point should be raised here regarding the appropriateness of measuring these rear grill surfaces. The foam shell being tested is proposed for use in conjunction with the GESS. Therefore, thermal measurements of the unsuppressed exhaust grill are somewhat academic in that they

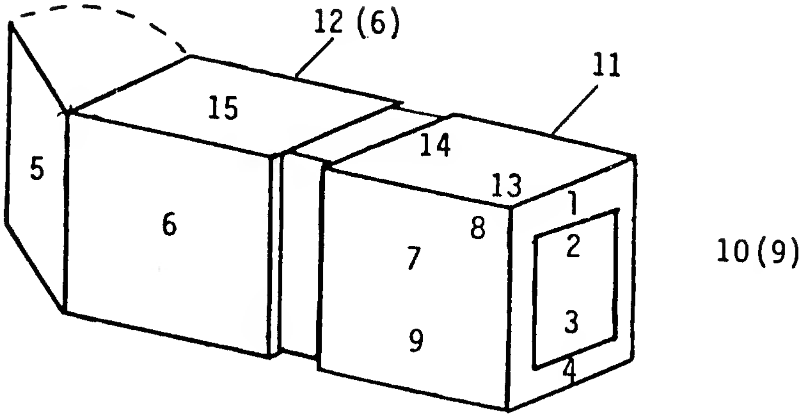

Figure A3. Points at which temperature measurements were taken on MEP 115A 60-kW diesel generator.

Table A1

PRT-5 and Thermocouple Raw Temperature Data Taken on AN/TPQ-37 MEP 115A 60-kW Diesel Generator*

TIME OF DAY	COMMENTS	POINTS														
		1	2	3	4	5	6	7	8	9	10	11	12	13	14	15
22 Oct 1980																
0850 hrs	5% Load	/62	60/64	60/65	/52	/17	21/20	42/43	50/52	50/45	/36	46/47	15/16	53/54	32/29	/18
0740/0730	5% Load	67/65	63/65	64/61	50/50	18/22	22/24	46/44	57/53	46/42	38/33	50/47	18/19	57/54	33/32	20/23
0805	5% Load	/65	/64	/65	/51	/23	/26	/46	/52	/46	/36	/48	/22	/55	/33	/26
0906/0930	5% Load	67/64	62/65	65/66	51/50	26/24	30/28	47/45	55/54	47/44	39/33	50/45	22/23	57/55	37/35	29/28
1023	Louvres open 5% Load-Cloudy	44/38	45/38	37/35	35/29	27/24	31/29	40/35	45/41	33/33	29/26	28/26	25/23	40/36	37/35	32/30
1114		42/	45/	36/	32/	26/	27/	35/	39/	30/	29/	28/	25/	36/	32/	28/
1215	5% Load	43/38	47/41	39/38	31/34	27/28	33/32	42/40	45/44	38/38	31/31	32/31	25/26	42/41	36/36	33/33
1315	5% Load	42/39	44/42	38/36	33/32	33/31	32/31	42/40	45/44	34/36	31/30	31/31	28/28	40/39	37/36	33/33
1400		36/33	41/34	33/28	26/23	29/24	29/24	35/32	39/34	31/28	25/22	23/22	21/21	33/30	28/24	25/23
1523	5% Load	35/30	40/32	30/28	22/21	23/22	21/21	28/27	33/28	27/26	21/21	20/21	18/19	28/27	19/19	19/19
1632	5% Load	30/24	37/28	28/23	18/18	16/15	16/16	21/19	27/23	20/19	18/17	17/16	15/15	25/23	15/15	14/15
1734	5% Load	27/24	36/26	26/23	16/16	14/12	16/13	22/16	26/21	19/16	16/15	18/14	15/12	23/20	15/12	15/12
1900	5% Load	26/23	37/27	24/19	15/13	13/12	13/12	16/16	21/20	17/15	16/15	15/16	13/14	22/21	12/12	12/13
2022	5% Load	27/22	32/24	23/17	14/13	12/12	12/12	15/14	21/17	15/14	16/14	14/13	12/12	22/19	11/10	11/11
2225	5% Load	23/19	30/22	20/18	11/10	10/8	10/9	14/12	20/16	14/11	13/11	12/11	10/8	19/17	9/7	9/8
23 Oct 1980																
0026	5% Load	22/15	27/18	19/16	10/12	8/8	8/7	12/11	18/15	12/11	12/11	10/11	8/8	16/16	7/7	6/7
0226	5% Load	20/14	26/16	16/14	8/10	7/5	6/5	11/9	16/13	10/9	11/9	9/9	7/6	18/14	5/5	5/5
0420	5% Load	20/16	25/17	15/14	8/8	7/6	8/5	10/8	15/12	12/8	11/8	10/7	7/7	17/14	6/4	6/4
0520	5% Load	20/16	26/19	16/14	7/7	6/5	5/5	9/8	16/14	10/9	10/8	8/7	6/5	17/14	5/5	4/5
0607	5% Load	23/17	28/20	17/14	15/11	7/4	8/5	11/8	15/14	12/9	9/7	9/6	6/4	17/14	6/4	5/5
0705	5% Load	24/21	28/22	18/17	20/19	8/7	9/7	15/15	21/17	14/12	11/10	10/10	7/7	19/15	10/9	8/8
0750hrs	5% Load	28/23	30/24	25/19	28/22	9/8	13/10	20/17	23/21	18/14	13/12	12/11	10/8	22/19	14/13	13/11

* Data are tabulated as PRT-5/thermocouple readings.

are irrelevant to the current study, although they do demonstrate the need for the GESS. Therefore, these surfaces were not included in the thermal models, nor were conclusions as to the performance of the foam based on them. However, since the data were taken, they are presented.

Measurements of the camouflaged generator were made in the same manner as for the stock unit. Figure A4 shows the location of the representative points, whereas Table A2 contains the PRT-5 and thermocouple raw data. It should be pointed out that no points on the foam shell had contact temperatures taken due to constraints described in Chapater 2 relating to thermal properties of the surface. It was virtually impossible to obtain good heat conductivity either within the surface or between the surface and the probe because of the nature of the foam and its thin foil aluminum crinkle exterior. Since it was recognized that the contact thermocouple measurements would be useless, they were not made.

Another point should be made relating to the discussion in Chapter 2. Field measurements indicated the aluminum crinkle foil had a nonnegligible thermal reflectivity, and it was obvious that PRT-5 measurements made for this material were significantly influenced by what was reflected in the surface. More of this subject will be discussed later in conjunction with laboratory reflectance measurements made for the aluminum and bare foam materials. At this point, however, let it be said that the only accurate thermal measurements of the camouflage shell were obtained at points where the foil had been stripped off to expose the much less reflective foam surface. Table A3 presents the background and weather data for the test.

Material Infrared Properties

The need to measure the material's infrared optical properties was clear from the field tests. For this reason, PRA subcontracted to Surface Optics Corporation for laboratory measurements of the white crinkle foil and the bare foam. The results are shown in Figures A5 through A8. These measurements confirmed initial suspicions about the white foil, i.e., that it has a fairly high (.5) reflectance in the 8 to 14 micron region,

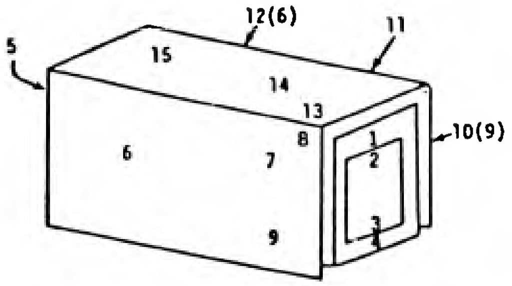

Figure A4. Points at which temperature measurements were taken on MEP 115A 60-kW camouflaged diesel generator.

Table A2

Raw Temperature Data Taken for 60-kW Diesel Generator with Camouflage Shell*

TIME OF DAY	COMMENTS	POINTS														
		1	2	3	4	5	6	7	8	9	10	11	12	13	14	15
October 22																
0640	60% LOAD	29/	33/48	33/48	25/	14/	/16	/16	/16	/14		/14	/12	/16	/15	/15
0740/0720	30% LOAD	41/37	41/43	34/43	30/32	19/18	/19	/18	/18	/18	/18	/20	/19	/18		/15
0800	25% LOAD	34/	42/	37/	32/	21/										
0900	25% LOAD	37/42	45/47	38/42	23/23	/27	/26	/26	/26 /27	/28	/24	/24	/24	/28	/28	/28
1012	60% LOAD	37/42	47/54	45/50	31/38	23/25	/27	/27	/20 /30	/30	/31	/27	/30	/31	/29	/29
1110	60% LOAD	/39	/55	/48	/32	/25	/32	/34	/34 /36	/33	/30	/30	/29	/32	/30	/30
1210	60% LOAD	38/40	45/52	44/50	31/30	26/25	/36	/34	/34 /38	/35	/31	/31	/30	/32	/32	/32
1310	25% LOAD	38/40	47/48	43/45	35/31	29/27	/36	/37	/36 /42	/35	/41	/41	/30	/32	/32	/32
1405		28/35	41/46	36/44	25/25	20/20	/22	/21	/25 /26	/21	/21	/19	/19	/20	/19	/20
1522	60% LOAD	29/35	41/46	36/44	25/25	20/20	/22	/21	/22 /25	/21	/21	/19	/19	/20	/19	/20
1624	60% LOAD	32/32	40/44	32/42	24/21	16/15	/16	/17	/18 /16	/18	/16	/16	/16	/13	/13	/13
1724		29/32	39/45	33/35	21/21	12/15	/17	/13	/18 /16	/16	/16	/17	/16	/13	/14	/13
1850	60% LOAD	25/25	38/41	31/37	20/18	14/13	/13	/14	/14 /12	/16	/17	/12	/13	/15 /17	/13	/15
2017	60% LOAD	22/29	38/45	29/34	18/17	13/12	/14	/14	/15 /11	/14	/13	/11	/14	/16	/14	/13
2215	60% LOAD	22/29	38/45	29/34	19/17	13/12	/14	/14	/15 /11	/14	/13	/11	/14	/16	/14	/13
October 23, 1979																
0020	60% LOAD	15/23	30/41	28/35	14/14	9/10	/13	/11	/8 /9	/10	/10	/10	/13	/13	/12	/10
0212	60% LOAD	13/20	23/34	21/26	9/9	5/6	/7 /5	/6	/7 /4	/7	/5	/5 /5	/5	/5	/6 /1	/4
0412	60% LOAD	12/20	25/36	23/29	14/10	5/8	/6 /5	/7	/8 /5	/7	/5	/10 /6	/8	/8	/10 /3	/5
0515	60% LOAD	14/20	30/36	23/25	12/8	5/5	/7 /4	/6	/6 /4	/6	/7	/7 /3	/8	/6	/7 /0	/4
0603	60% LOAD	18/21	28/45	23/32	11/12	4/6	/9 /4	/8	/8 /5	/8	/9	/8 /5	/9	/9	/9 /2	/10
0700	60% LOAD	20/25	33/40	24/30	18/16	6/7	/8 /6	/9	/9 /7	/8	/7	/8 /6	/7	/8	/6 /4	/6
0745	60% LOAD	25/30	33/40	26/32	20/23	8/9	/12 /10	/11	/14 /11	/12	/13	/10 /8	/11	/12	/12 /10	/13

*Data are tabulated in °C as thermocouple/PRT-5 radiances.

Table A3

Test Site Background and Weather Data--Fort Sill, Oklahoma

TIME	AIR TEMPERATURE		WIND SPEED (mph)	WIND DIRECTION	BACKGROUND (°C)			
	DRY BULB (F°)	WET BULB (F°)			SCRUB		SOIL	
					Sun	Shade	Sun	Shade
22 October 80								
0710	59	56			13		12	
0748	67	60	8-10	S	19		18	
0837	64	62	8-10	S			23	
0915							27	20
0935	71	62	15	S				
1000							31	21
1027	72	62	12-15	S	28		31	
1100					26		30	
1150	70	60	7	S	33		33	
1255	76	61	0-5	SSW	32		33	
1320					34		35	
1345	72	60	15-25	NW	20		25	
1510	64	52	20-25	N			22	
1530							19	
1610	59	47	20-25	N			12	
1640							15	
1705	56	45	15-25	N				16
1835	54	44				13		13
1905			17-23	N		12		11
2000	51	42	8-14	N		12		10
2025						12		10
2200	49	42	5-10	N		10		9
23 October 80								
0000	45	40	5-8	N		8		6
0200			0-3	N		7		5
0300	40	36						
0400			0-3	N		6		5
0500	40	35	5-8	NW		7		5
0530	39	34						
0550	38	34	3-6	NW		5		4
0645	42	36	6-9	NW	7	6	6	5
0710	44	37			10	7	8	7
0730	45	39	6-9	NW				
0755					10	9	12	7

SUNSET 22 OCTOBER 1980 @ 1647 HOURS
SUNRISE 23 OCTOBER 1980 @ 0547 HOURS

SCATTERED CLOUDS OVER TEST SITE
22 OCTOBER FROM 1000 HOURS TO 1300 HOURS

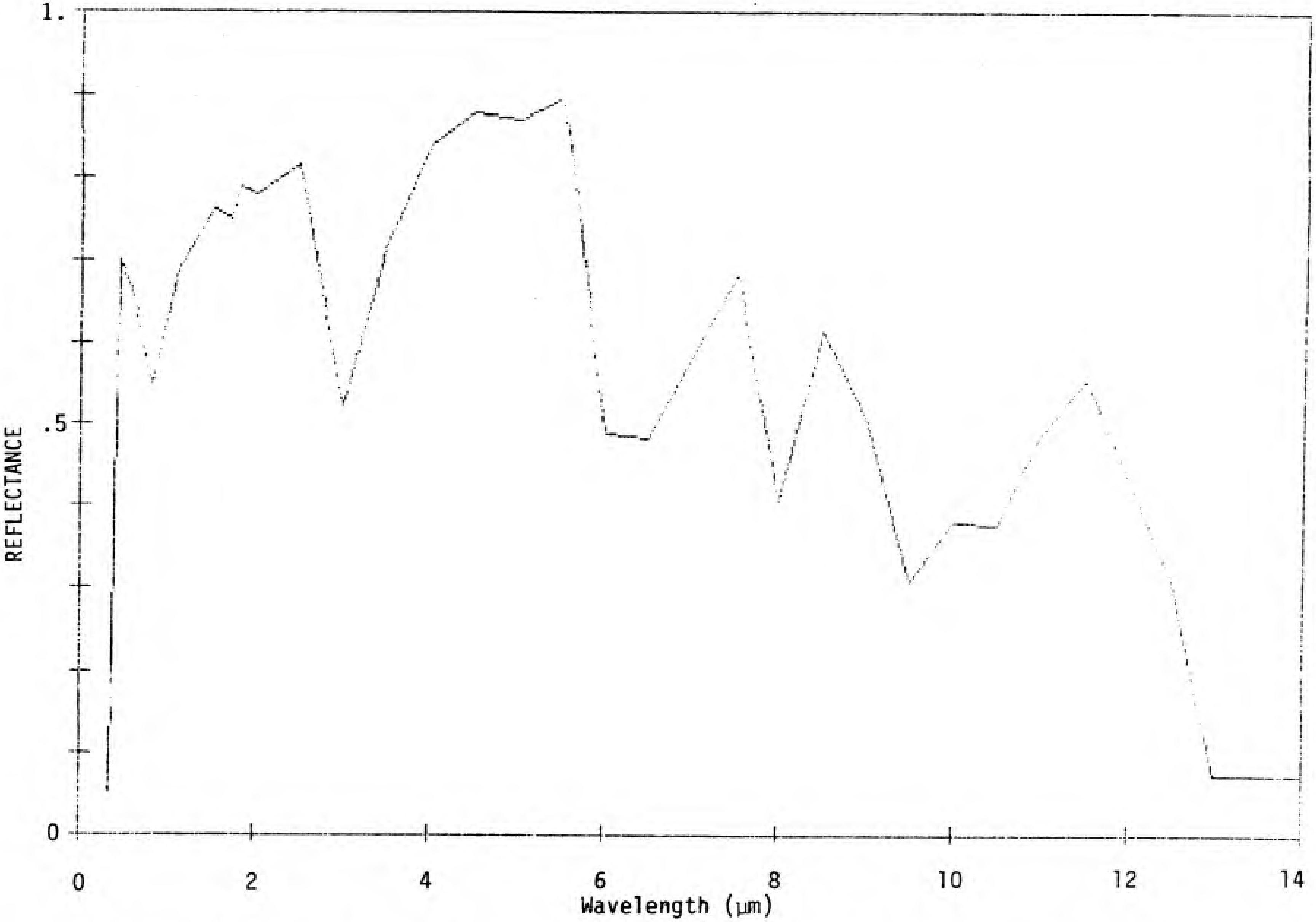

Figure A5. White crinkle aluminum foil diffuse reflectance vs wavelength, $\Theta_i = 20°$.

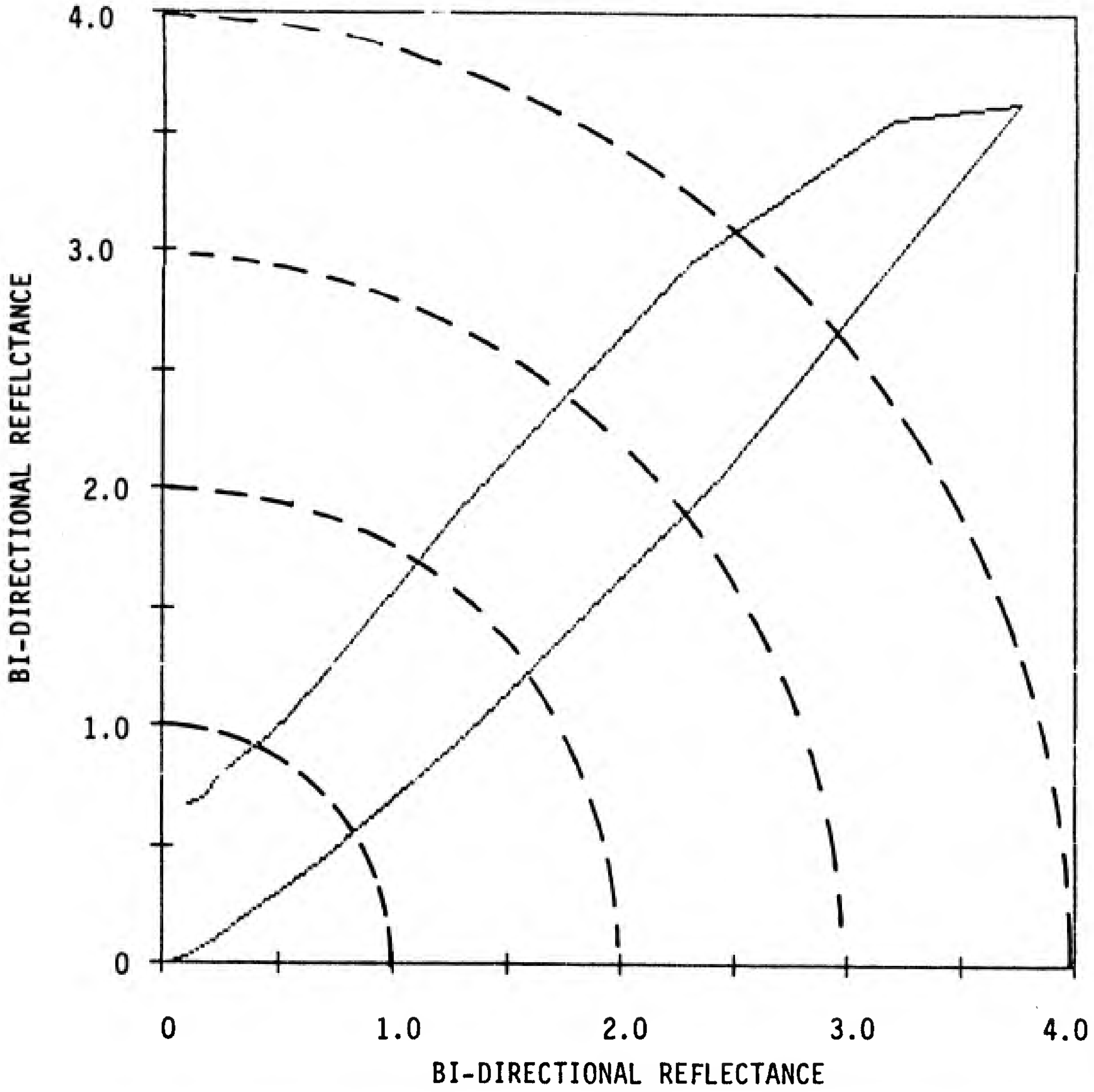

Figure A6. Bidirectional reflectance for white aluminum crinkle surface. Polar plot for reflectance vs Θ_r for Θ_r between 0 and 90 degrees. $\Theta_i = 45°$; $\theta = 180°$; $\lambda = 10\ \mu m$.

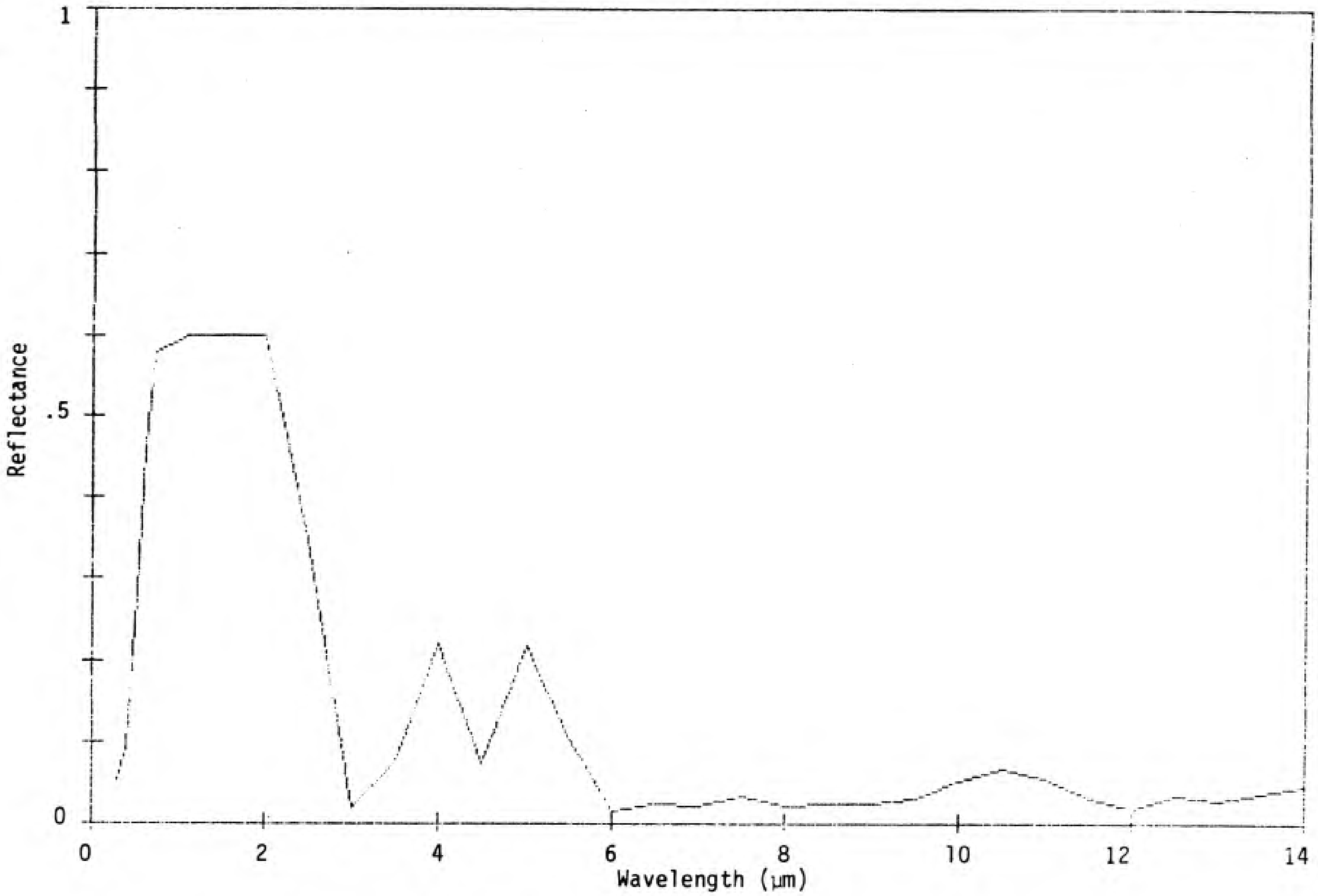

Figure A7. Foam diffuse reflectance vs wavelength, $\Theta_i = 20°$.

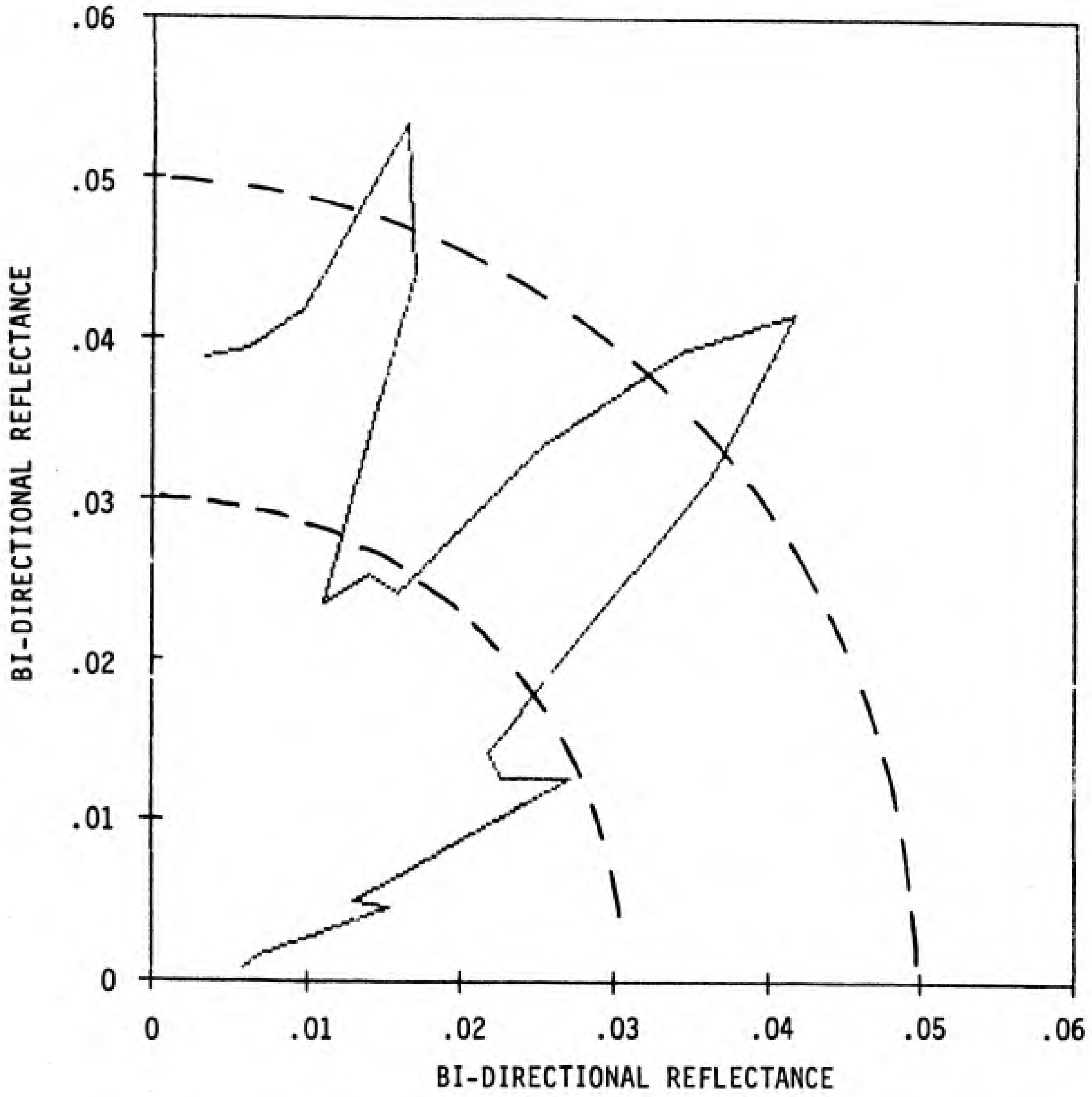

Figure A8. Bidirectional reflectance for bare polyurethane foam. Polar plot for reflectance vs Θ_r for Θ_r between 0 and 90 degrees. $\Theta_i = 45°$; $\Theta = 180°$; $\lambda = 10$ μm.

and furthermore that it is extremely specular (see Figure A5). These attributes describe a fair infrared mirror. The fact that reflectivity is only .5 implies that the reflected image would appear somewhat dimmer than it would in a perfect mirror, but the specularity of the surface is such that the image appears fairly sharp. Direct use can be made of such a surface, as will be discussed below.

The foam surface, on the other hand, has a much lower reflectance (see Figure A7) than the foil, and furthermore, its surface is rather diffuse, as shown in Figure A8.

GESS Thermal Data

Since the baseline for comparison between the suppressed and unsuppressed generators was the 60-kW diesel unit with GESS, and none had been available during the field test, use was made of the BLUE FISH data taken on 10-11 October 1979 at Fort Hood.[1]

The data gathered for an operating 60-kW with GESS appears to be consistent and of good quality. All measurements were made with a PRT-5. Figure A9 shows the locations of their representative points, and Table A4 contains the raw data taken for the 2 days.

---

[1] TCATA/3rd Corps Field Test. Data made available by Dr. Gandy, Fort Hood, Texas.

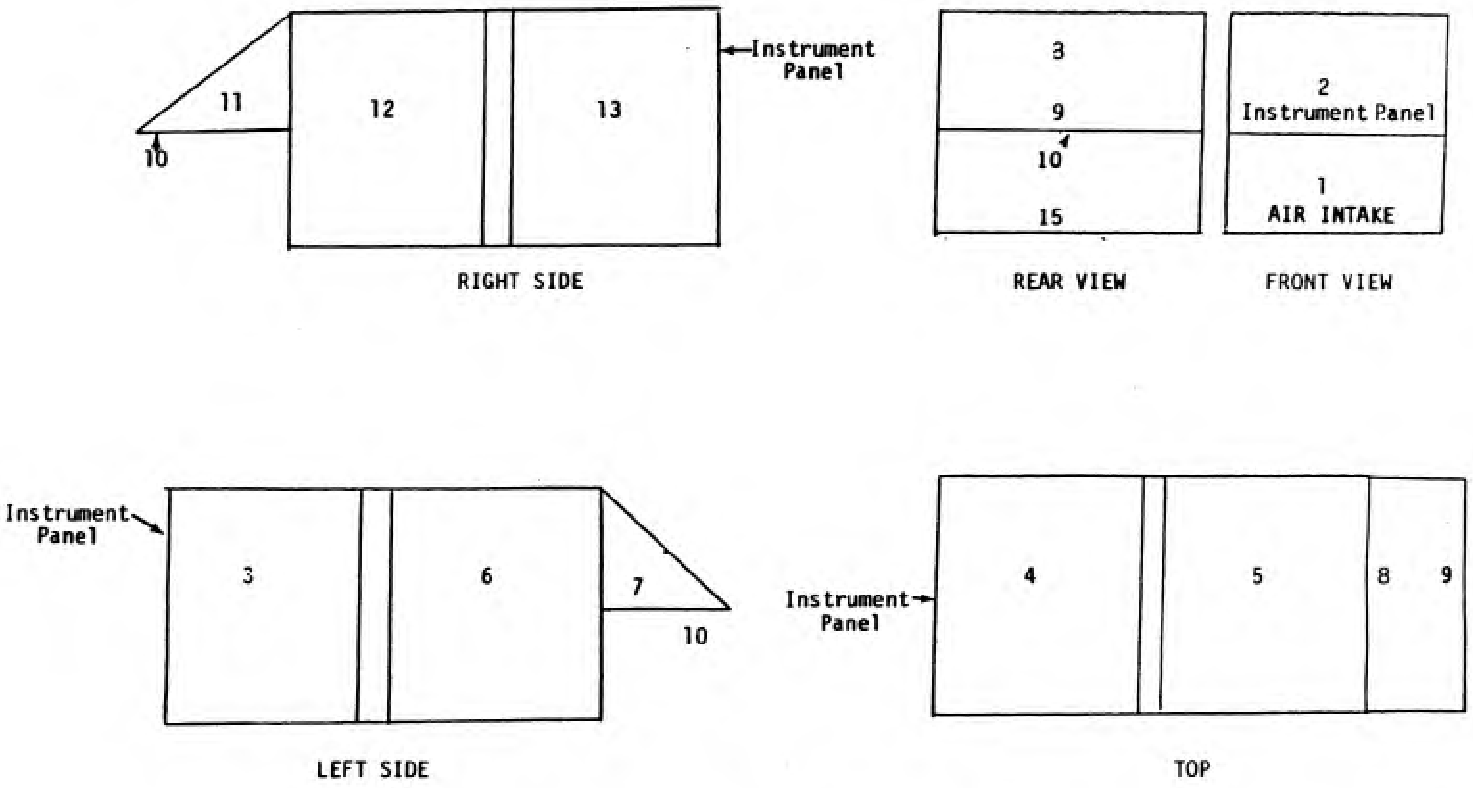

Figure A9. Schematic diagram of 60-kW diesel generator with GESS.

(Supplied by Dr. Gandy, from Fort Hood, Texas, TCATA/3rd Corps Field Test.)

Table A4

PRT-5 Temperature Data (°C) Taken for Representative Points (See Figure A5) of 60-kW Diesel with GESS.*

	October 10, 1979				October 11, 1979				
	1230	1430	1630	1830	1400	1600	1800	2020	2218
1	30	34	32	27	23	24	20	14	15
2	34	38	33	30	27	25	21	16	16
3	30	34	33	28	25	23	22	15	13
4	32	37	33	28	25	23	23	14	13
5	37	37	32	27	29	25	27	17	16
6	33	35	33	29	26	25	21	18	16
7	33	36	34	29	27	25	21	20	16
8	35	37	33	28	30	27	30	19	19
9	36	41	34	29	31	28	32	19	23
10	66	67	65	79	67	65	51	52	47
11	39	42	38	37	36	31	25	19	21
12	39	43	38	37	33	28	24	18	18
13	36	39	37	32	45	24	23	18	14
14	41	46	40	43	36	35	26	24	16
15	41	42	43	44	43	32	27	26	16

---

*TCATA/3rd Corps Field Test. Data supplied by Dr. Gandy, Fort Hood, Texas.

4 DATA REDUCTION

The evaluation of the foam camouflage material in this study is based on the reduction in infrared vulnerability offered to a 60-kW diesel generator with GESS by a shell of the proposed foam. For this comparison it is necessary to develop thermal models of the baseline generator and of any camouflage schemes to be considered.

Baseline Model

The simulation of the GESS was done by computing the average temperature distribution measured at Fort Hood with respect to the adjacent surfaces. Figure A10 shows this synthetic GESS, along with the necessary temperature differentials obtained by a least-square fit from the Fort Hood data. The large standard deviation with respect to the mean value indicates these fairly small temperature differentials are not significant.

This procedure produced a satisfactory baseline as shown in Figure A11. It was then possible to make comparisons of camouflage shells of different material compositions with the baseline.

Proposed Camouflage Shell Designs

Three shell compositions have been considered: (1) aluminum-surfaced foam only, (2) bare foam only, and (3) bare foam top and aluminum-covered foam sides. The reason for choosing these three candidate compositions was based on the fact that the aluminum coating was a very good reflector; thus, shells with the coating on the sides appeared to mirror the environment, providing very good camouflage. If also used on the top of the target, this valuable characteristic of high reflectance became a liability. The black sky was usually reflected, producing a large negative contrast for the target. During the day, the situation could have arisen in which the observer was right at the specular point of the solar reflected radiance and could have

Average Thermal Differences

(°C)

QUANTITY	AVERAGE	STANDARD DEVIATION
$\left(T_{A_1} - T_A\right)$	.6	.7
$\left(T_{B_1} - T_B\right)$	1.2	1.56
$\left(T_{B_2} - T_B\right)$	2.9	2.3
$\left(T_{C_1} - T_C\right)$	1.1	1.5

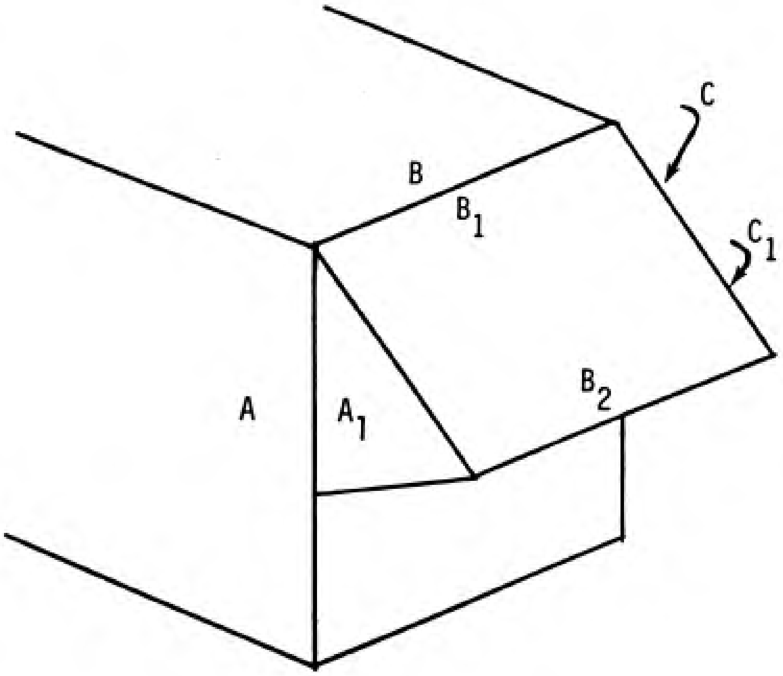

Figure A10. Temperature distribution of the GESS. Average temperature differentials measured between the given pairs of temperature points are listed. (Data supplied by Dr. Gandy, Fort Hood, Texas, from the TCATA/3rd Corps Field Study.)

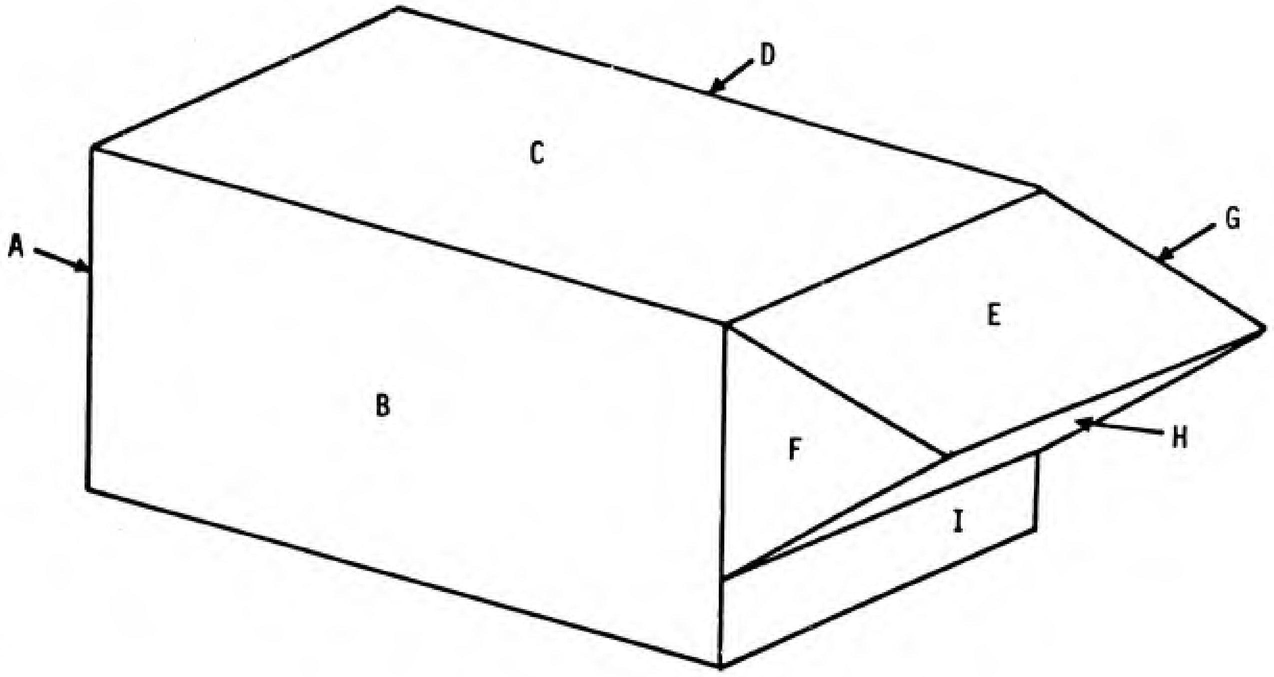

		APPARENT ΔT C°	
SURFACE	AREA (M^2)	0 HRS.	1300 HRS.
A	1.31	1	0
B	2.31	3.2	3.7
C	1.85	1.8	3.4
D	2.31	3.0	3.7
E	1.03	3.8	5.4
F	.34	3.7	4.3
G	.34	4.0	2.7
H	.75	19.0	9.0
I	.33	3.0	0

Figure A11. Baseline target with GESS. Shown for each indicated surface is its area (m^2) and apparent ΔT (°C) for two times of day.

seen an extremely large glint. For these reasons, it was decided to include a third composite shell of aluminum-coated sides and a bare foam top in addition to considering the simple shells of bare foam and aluminum-coated foam.

Base Foam Shell

The creation of target model facets covered by bare foam was straightforward. There were sufficient data collected at bare foam points during the field measurements to allow the synthesis of a bare-foam model.

The validity of these measurements was confirmed by creating a dynamic equilibrium heat balance model of a material whose physical properties matched those of the foam material. Comparison of the measured data with the temperatures predicted by this model is a good indicator of both model and measurement reliability. As shown in Figure A12, the agreement is remarkably good. The discrepancy between 4:00 p.m. and midnight is due to the fact that the model uses a constant wind velocity and has been corrected for the target models. The congruence of these diurnal temperatures is a strong indication that: (1) the apparent temperature measurements obtained by PRT-5 are accurate, and (2) the material properties are adequately represented by the model.

The model shows that the thermal insulation provided by the foam is very good; not surprisingly, there was virtually no heat flux between the inside and outside surfaces. Figure A13 shows the thermal model of the bare foam camouflaged generator.

Aluminum-Surfaced Foam Shell

Since there were no reliable temperature measurements of the foil-covered foam (due to the limitations discussed in Chapters 2 and 3), it was necessary to synthesize apparent temperatures of this material. These were calculated using the dynamic equilibrium heat balance model. The bare foam

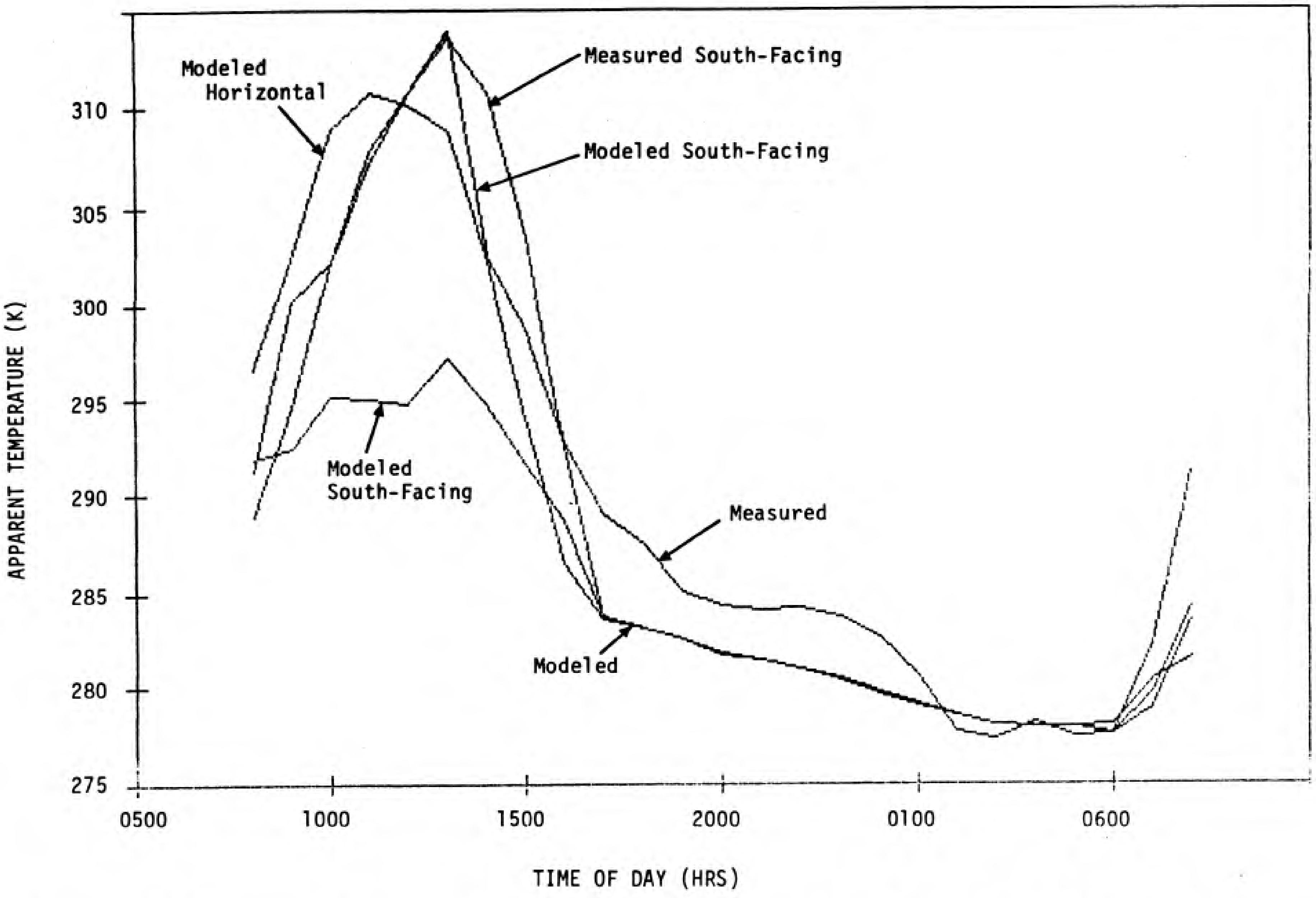

Figure A12. Measured and synthesized bare foam apparent temperatures; measured data for south side; synthesized data for south, top, and north sides.

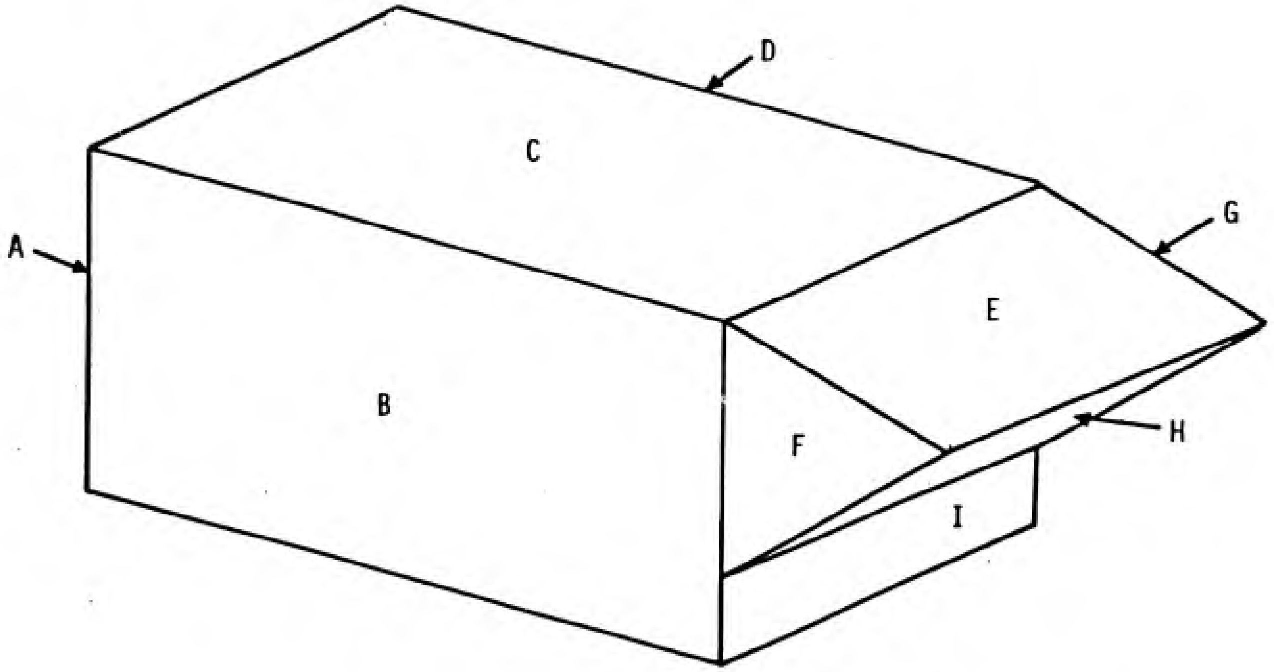

SURFACE	AREA (M^2)	APPARENT ΔT C° 0 HRS.	 1300 HRS.
A	1.7	1.0	0
B	2.48	2.4	7.3
C	2.21	2.3	2.5
D	2.48	2.4	-9.1
E	1.23	2.3	2.5
F	.37	2.4	7.3
G	.37	2.4	-9.1
H	.92	19.0	9
I	.39	3.0	0

Figure A13. Bare foam shell target model. Shown for each indicated surface is its area (m^2) and apparent ΔT (°C) for two times of day.

material description was modified to accommodate optical properties of aluminum skin, and temperatures were estimated for the diurnal cycle. These actual temperatures were then converted to apparent temperatures (Figure A14) using Equation A1. The results were used to produce the aluminum-surfaced foam target model shown in Figure A15.

Composite Shell

The final candidate target, the composite bare foam/aluminum-surfaced foam, was derived from the aluminum-surfaced foam target model by substituting the bare foam facet temperatures for the two upward pointing faces C and E (compare Figures A15 and A16). It has been assumed that the sun glint off any facet was not observed, since the probability of this event is very low.

Asymmetries in the temperatures occurred because the target was oriented the same way it had been in the field. The major side-to-side differences were observed during the day and were caused by the position of the sun, which illuminated face B while face D was in shade.

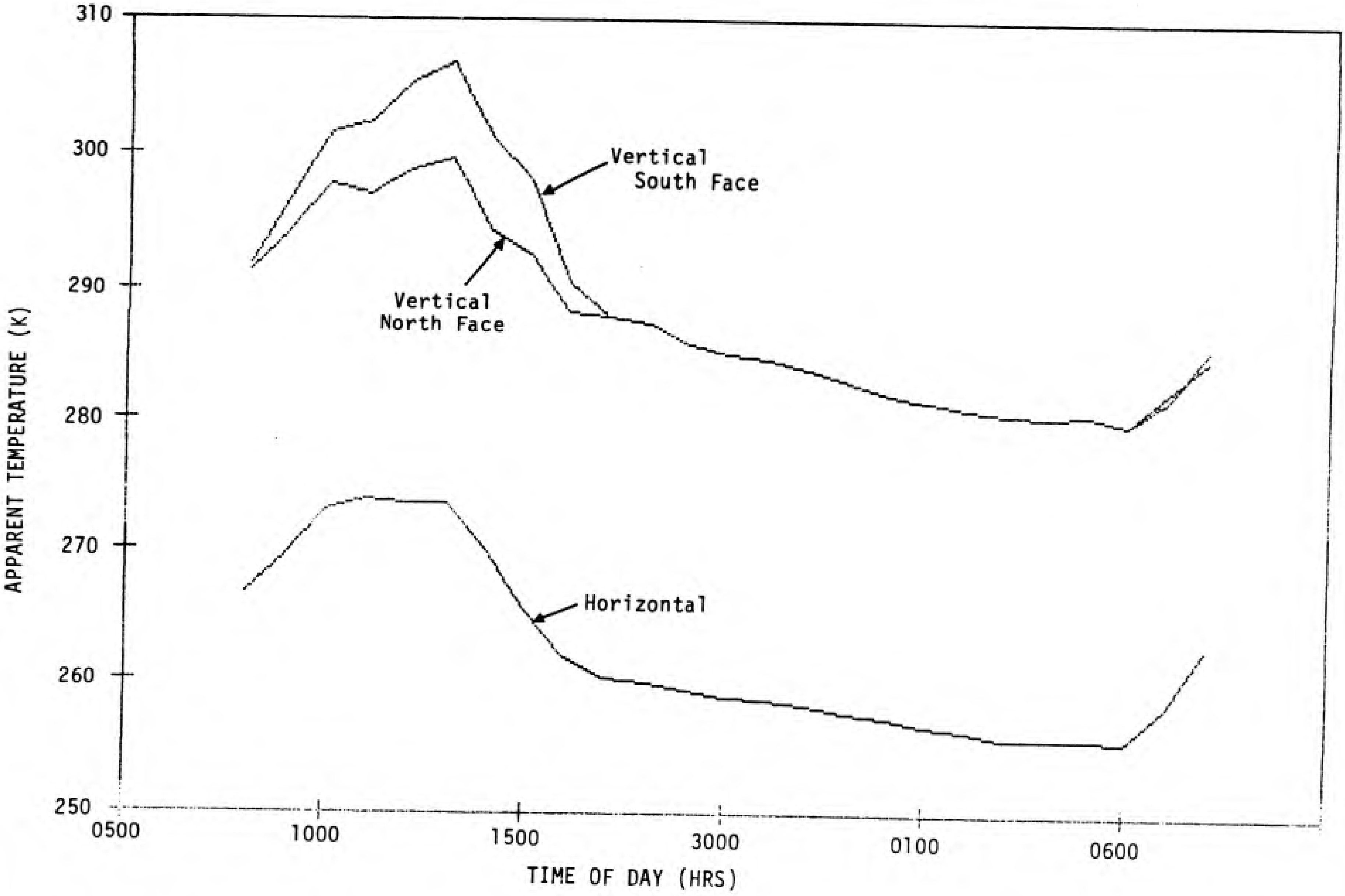

Figure A14. Synthesized aluminum-surfaced foam apparent temperatures for the shell south, top, and north sides.

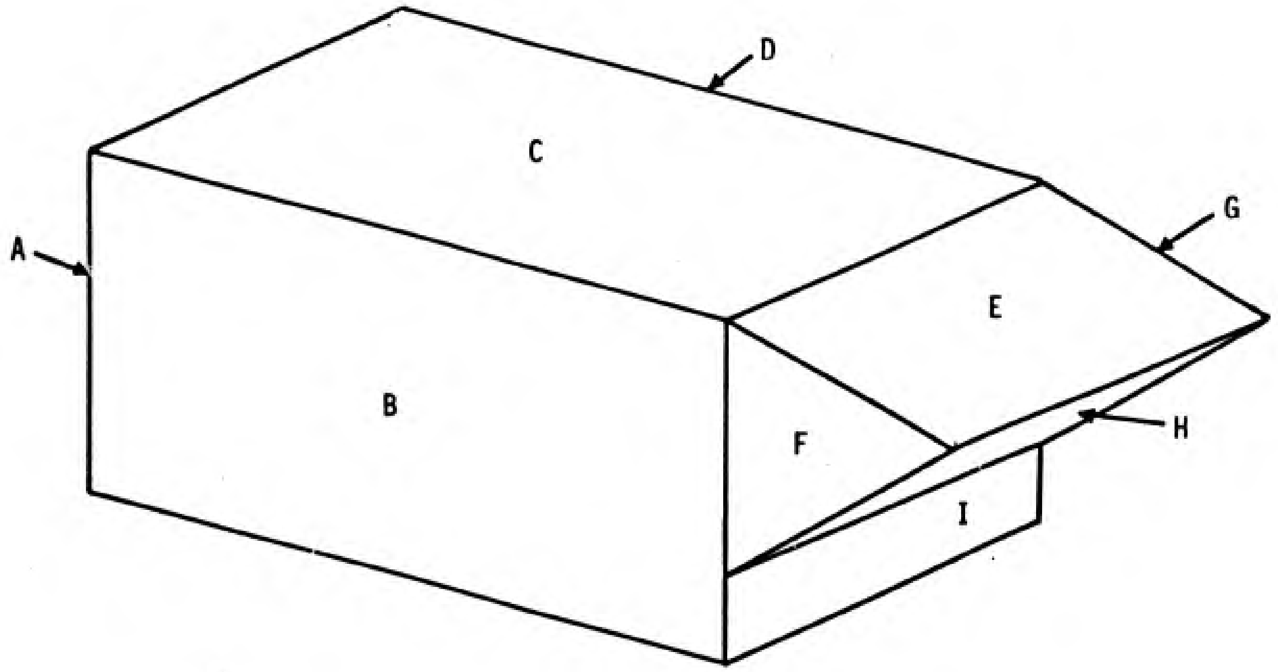

SURFACE	AREA (M^2)	APPARENT ΔT C° 0 HRS.	1300 HRS.
A	1.7	1.0	0
B	2.48	1.8	0.3
C	2.21	-33.0	-32.9
D	2.48	1.8	-6.6
E	1.23	-33.0	-32.9
F	.37	1.8	0.3
G	.37	19.0	9.0
I	.39	3.0	0.0

Figure A15. Aluminum-surfaced foam shell target model. Shown for each indicated surface is its area (m^2) and apparent ΔT (°C) for two times of day.

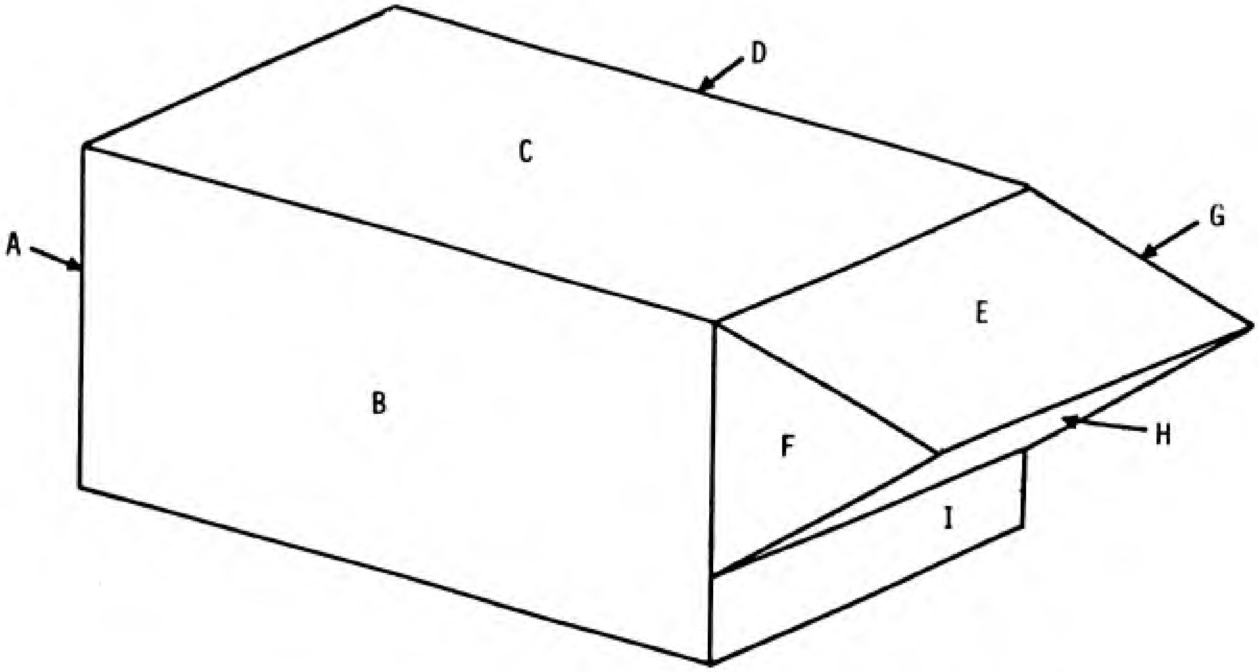

		APPARENT ΔT C°	
SURFACE	AREA (M^2)	0 HRS.	1300 HRS.
A	1.7	1	0
B	2.48	1.8	0.3
C	2.21	2.3	2,5
D	2.48	1.8	.6
E	1.23	2.3	2,5
F	.37	1.8	0.3
G	.37	1.8	-6,6
H	.92	19	9
I	.39	3	0

Figure A16. Composite bare foam/aluminum-surfaced foam target model. Shown for each indicated surface is its area (m^2) and apparent ΔT (°C) for two times of day.

5 DATA ANALYSIS

Detection Estimation

The basis for comparison of the four target models is the range at which each is detectable by a given sensor under a variety of conditions. The technique used to estimate the detection range is based upon Ricean detection criteria.[2] This method assumes that an unresolved target is imbedded in a Gaussian noise background.

A brief discussion will be presented of the method used to calculate the necessary signal-to-noise ratio for a specified probability of detection at a given false alarm rate. This will be followed by a cursory description of the sensor performance model and a derivation of the noise figures of the total system for the scenarios being considered. At this juncture, the required target intensity contrasts for detection are available, and the remainder of this section contains estimations of detection ranges for the various scenarios.

These calculations have been carried out assuming an unresolved target or, more exactly, a target that exactly matches the system IFOV. This analysis will, therefore, approximate the performance of the best unresolved systems. For this reason, the results should be taken as representative of a middle range of sensor discrimination capabilities--better than those in which the target does not fill an IFOV and worse than those high resolution systems for which the target subtends many IFOVs.

More important than the absolute detection ranges estimated for a specific system is the relative performance of each of the candidate shell designs. For this purpose, the sensor treatment as described is entirely adequate.

The probability of detection can be expressed as a function of signal-to-noise ratio once the false alarm rate has been specified. The false alarm rate for a point target can be expressed as:

---

[2] S. O. Rice, "The Mathematical Analysis of Random Noise," Bell System Technol. J., Vol. 23 (1944), pp. 282-332; Vol. 24 (1944), pp. 146-156.

$$R_{fa} = N_{fa_a} * A_{IFOV}/A_{FOV} \qquad \text{[Eq A7]}$$

where N_{fa_a} is the number of acceptable false alarms per theater scan

A_{IFOV} (m^2) is the area of the instantaneous field of view

A_{FOV} (m^2) is the area of the entire theater scan.

This R_{fa}, in turn, can be used to calculate a detector threshold that will encounter the specified R_{fa} by the following expression:

$$R_{fa} = \frac{1}{\sigma\sqrt{2\pi}} \int_T^{\infty} e^{\frac{(x-x_o)^2}{-2\sigma^2}} dx \qquad \text{[Eq A8]}$$

where the integral, the Gaussian distribution function for a standard deviation of σ, and mean of x_o are integrated between the limits of the threshold T and infinity. This function cannot be inverted in closed form to obtain T, the signal-to-noise threshold. However, numerical solutions are straightforward, and the results of one such iterative method are presented in Figure A17.

At this point, we have come as far as being able to specify the signal-to-noise ratio necessary to achieve a given probability of detection, given a certain false alarm rate. To establish absolute intensity contrast thresholds, it is necessary to first determine the total system noise equivalent intensity. This determination can become exceedingly complex, but for the purpose of this study, simplifications can be made due to (1) the lack of advanced signal processing in the defined sensor threat and (2) the Gaussian background assumption.

In general, noise sources can be segregated according to the dimensions for which they are uncorrelated (i.e., time and/or space). For this analysis, it is adequate to consider two classes—temporally variant and spatially variant noises. In the first class are photon noise, detector

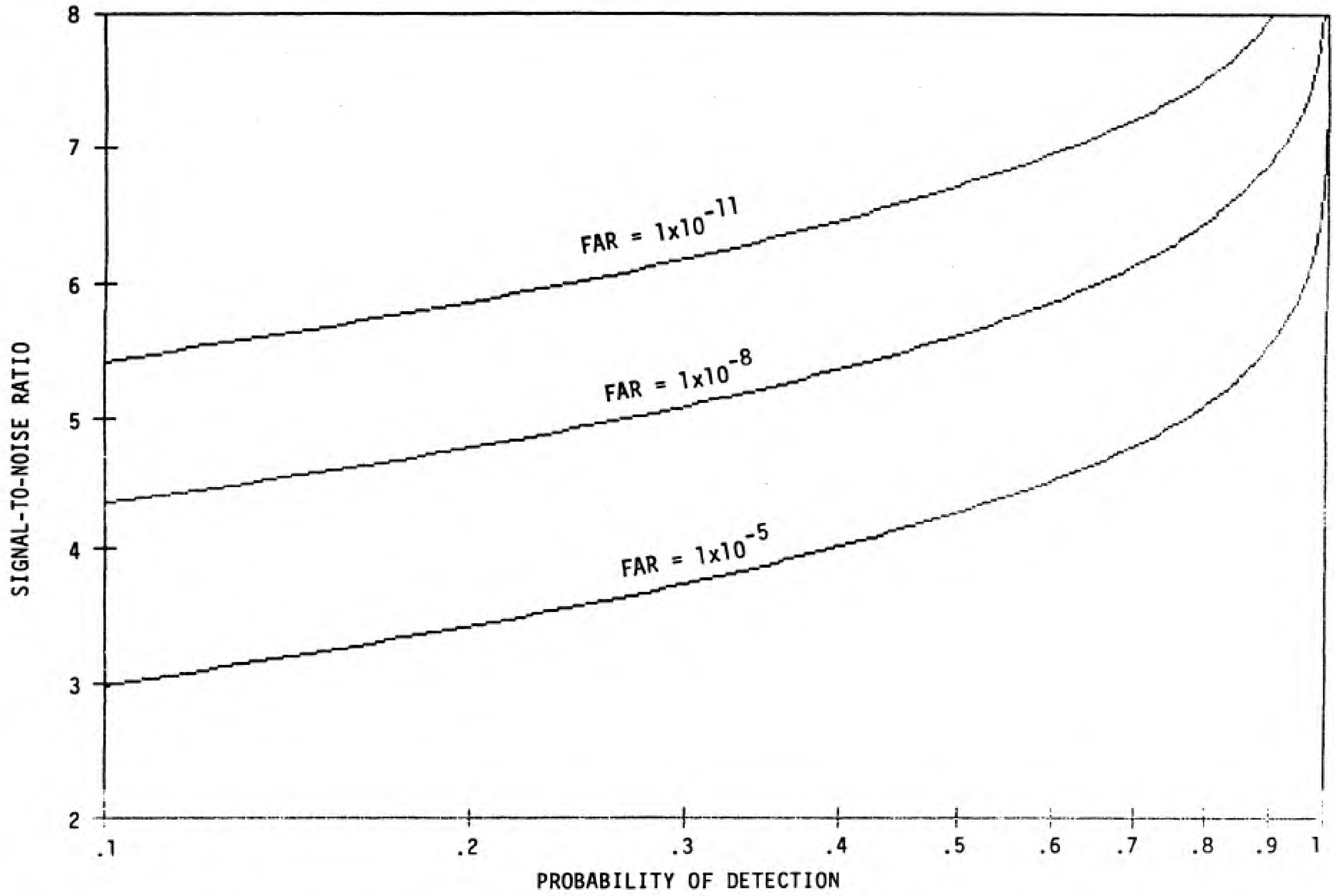

Figure A17. Signal-to-noise ratio vs probability of detection for three false alarm rates.

noise, shot noise, and numerous other specific time-variable noises that exist even when a sensor is facing an absolutely uniform background. For this study, the second class can be considered to consist solely of background clutter. Other spatial noises are introduced by sensor jitter, drift, and scan nonuniformities, but these are second order effects.

A sensitivity figure, expressed as resolvable ΔT, identifies the limit imposed on detection by the temporal (spatially constant) noise sources. The noise equivalent intensity contrast can be calculated as:

$$NEI_T = (N_{BB_{T_o}} - N_{BB_{T_o+\Delta T}}) * \Omega/R^2 \qquad \text{[Eq A9]}$$

where NEI $(w/cm^2/\mu m)$ is the noise equivalent intensity due to temporal noise

$N_{BB_{T_o}}$ $(w/cm^2/\mu m/sr)$ is the blackbody radiance at the background reference temperature

$N_{BB_{T_o+\Delta T}}$ $(w/cm^2/\mu m/sr)$ is the blackbody radiance of a surface at a minimally resolvable T from T_o

R(cm) is the range

Ω(sr) is the solid angle subtended by the instantaneous field-of-view.

The other important noise term, clutter, can also be presented in terms of NEI as:

$$NEI_C = \sqrt{2} * \sigma * N_{BB_{T_o}} * R^2 * \Omega \qquad \text{[Eq A10]}$$

where NEI_C is the noise equivalent intensity due to spatial noise

σ is the standard deviation of the background.

These terms are combined as:

$$NEI_{TOT} = \sqrt{NEI_T^2 + NEI_C^2} \qquad \text{[Eq A11]}$$

The background scenes must also be presented here so the integrated total system noise can be calculated for each scenario. Figure A18 presents the benign, low variability infrared background scene (Michigan conifers) used in this study. Shown in this figure are the intensity distribution functions[3] as measured for the scene at two times of day. The night distribution function shows that the scene is extremely uniform. This uniformity is only slightly reduced during the daytime by variations in solar reflectance, as shown in the intensity distribution function. At the opposite end of the background variability spectrum is the Camp AP Hill scene[4] (Figure A19), also measured at two times of day. This scene exhibits large, spatial radiance variability, especially during the day. The effects of these radiation variabilities will be demonstrated shortly.

Sensor and background data must be combined to establish a total system intensity contrast signal-to-noise ratio. Table A5 presents the intensity contrast thresholds of detection for the four scenarios.

The detection range is estimated for a specific scenario by iteratively solving for that range at which the apparent target contrast is equal to the threshold intensity contrast. For example, a sensor could be modeled as flying at an altitude of 1 km at an azimuth of 75°. The apparent target contrast is then computed at a series of ranges, taking into account the change in observer elevation angle measured at the target and the change in atmospheric transmission as a function of range. These apparent contrasts were calculated in the 8 to 12 micron band at a .5 micron resolution. Ranges at which the apparent target intensity contrast was equal to the threshold intensity contrast were found by iteration.

The baseline for all parametric comparisons is presented in Figure A20. The baseline case consists of an uncamouflaged generator (with a GESS)

---

[3] A. J. LaRocca and D. J. Witte, Handbook of the Statistics of Various Terrain and Water (Ice) Backgrounds from Selected U.S. Locations, ERIM Report No. 139900-1-X (1980).

[4] A. J. LaRocca and D. J. Witte.

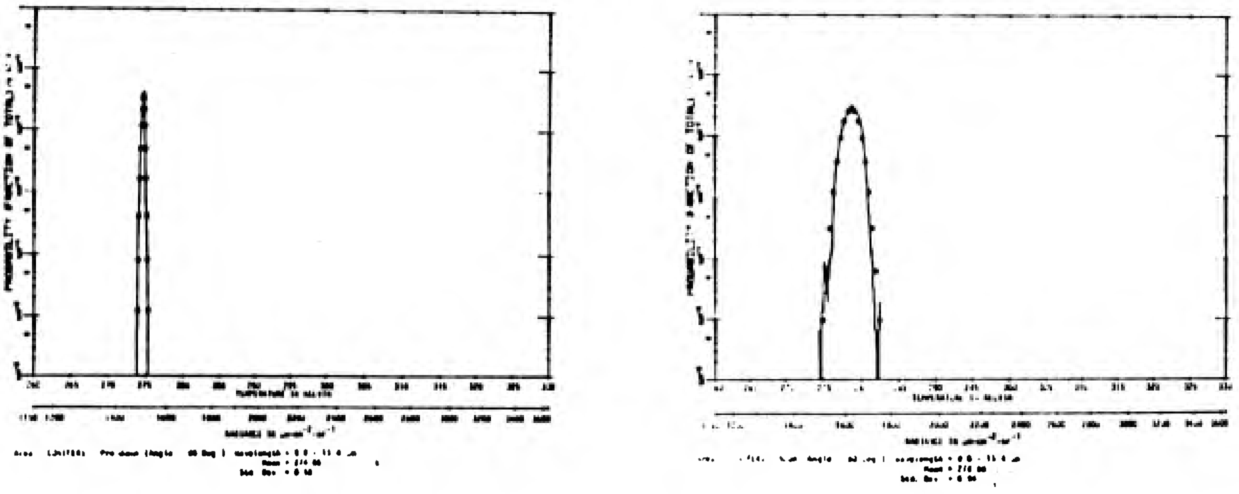

NIGHT

DAY

INTENSITY DISTRIBUTION HISTOGRAMS

Figure A18. Michigan conifer scene. (From A. J. LaRocca and D. J. Witte, Handbook of the Statistics of Various Terrain and Water [Ice] Backgrounds from Selected U.S. Locations, ERIM Report No. 139900-1-X [1980].)

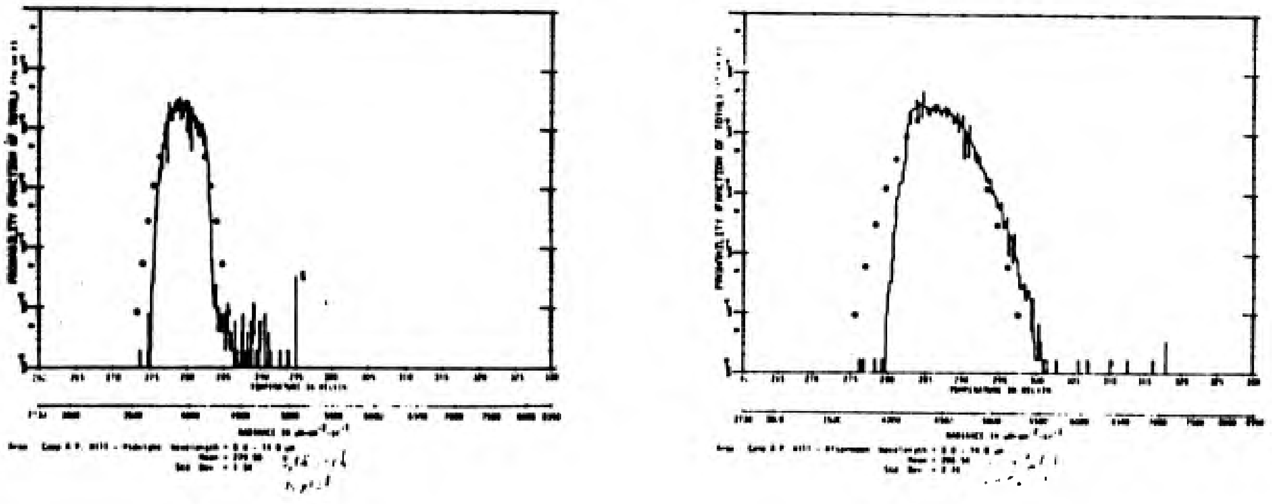

NIGHT

DAY

INTENSITY DISTRIBUTION HISTOGRAMS

Figure A19. Camp AP Hill Scene. (From A. J. LaRocca and D. J. Witte, Handbook of the Statistics of Various Terrain and Water [Ice] Backgrounds from Selected U.S. Locations, ERIM Report No. 139900-1-X [1980].)

Table A5

Noise Equivalent and Threshold Apparent Contrast Intensities

	Time of Day	NEI_t[1]	NEI_c[2]	NEI_{tot}[3]	ΔJ_T[4*]
Michigan Conifers	Night	$1.61x10^{-13}$	$4.42x10^{-13}$	$4.70x10^{-13}$	$2.63x10^{-12}$
	Noon	$1.61x10^{-13}$	$1.92x10^{-12}$	$1.93x10^{-12}$	$1.08x10^{-11}$
Camp AP Hill	Night	$1.61x10^{-13}$	$2.32x10^{-12}$	$2.32x10^{-12}$	$1.30x10^{-11}$
	Noon	$1.61x^{10-13}$	$5.23x10^{-12}$	$5.23x10^{-12}$	$2.93x10^{-11}$

*All values in units of $w/cm^2/\mu m$.

[1] Noise equivalent intensity due to spatially constant sources.

[2] Noise equivalent intensity due to spatially variant sources.

[3] Total system noise equivalent intensity (= $\sqrt{NEI_t^2 + NEI_c^2}$).

[4] Detectable apparent intensity contrast (= S/N_T[5] * NEI_{tot}).

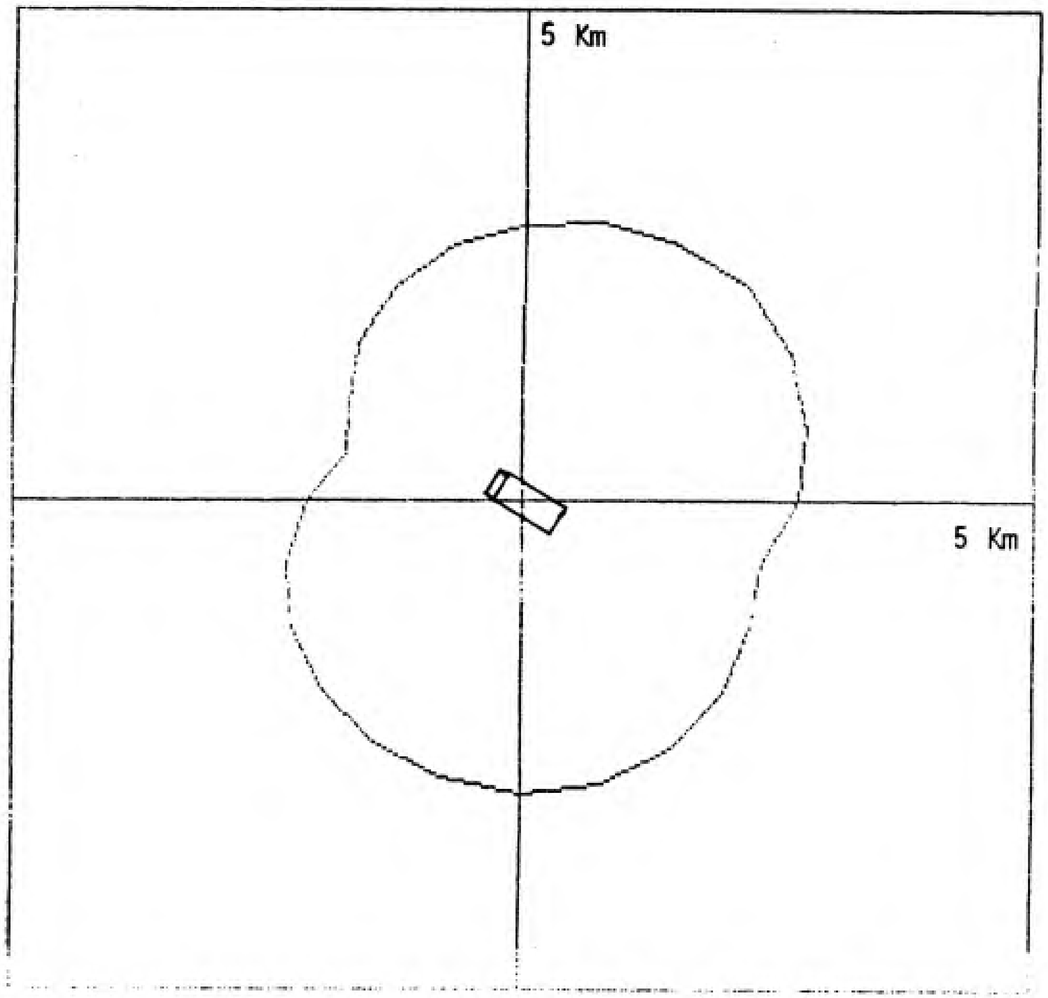

Figure A20. Baseline detection envelope. Camp AP Hill "noisy" background, 0 Hr, 60 kW with GESS. Probability of detection = .5. Midlatitude winter atmosphere. Sensor Alt = 1 km. Polar plot of detection range vs azimuth. North is up, east is right. All radial divisions are at 5-km intervals. Full scale = ± 5 km.

in the noisy AP Hill background, being overflown at an altitude of 1 km at night. The detection envelope is skewed with respect to the north-south axis because the generator model is oriented at a 20° clockwise rotation with respect to the east-west axis; this is illustrated by the schematic target located at the origin of the detection range plot (Figure A20). This figure shows the predicted detection range as a polar plot to present the azimuthal dependence clearly. It should be mentioned that every scale mark on all detection range plots represents a 5-km slant. Also, it should be emphasized that all ranges are slant ranges. In this case, the generator is least visible at a true azimuth of 285°, where its estimated detection range is 1.8 km. Its largest detection range is 3 km of slant at 180° true azimuth.

Figure A21 compares the vulnerability of the GESS-equipped 60-kW generator with that of the stock generator. The large lobe for the stock detection centered at 110° is the basic difference and is caused by the antagonist sensor's clear view of the hot exhaust area. The GESS reduces this critical detection range (where the sensor is directly aligned with the exhaust) by more than 50 percent. The penalty is slight; when the sensor confronts the side of the target, the detection range is minimally increased by the increase in target area due to the GESS.

The choice of this GESS-equipped 60-kW diesel generator as a baseline allows a clear-cut discussion of the real issues without an exhaustive parametric study. Before looking at the comparative performance of the various camouflage concepts, however, it is important to briefly review the basic parametric variables.

The first of these variables to be explored is probability of detection. Section A4 introduced this matter in the context of how threshold apparent target contrast was determined. Figure A22 shows detection envelopes for the baseline case as well as a higher and lower probability of detection. Clearly, for these conditions and assumptions, this variation in P_d is not of great consequence.

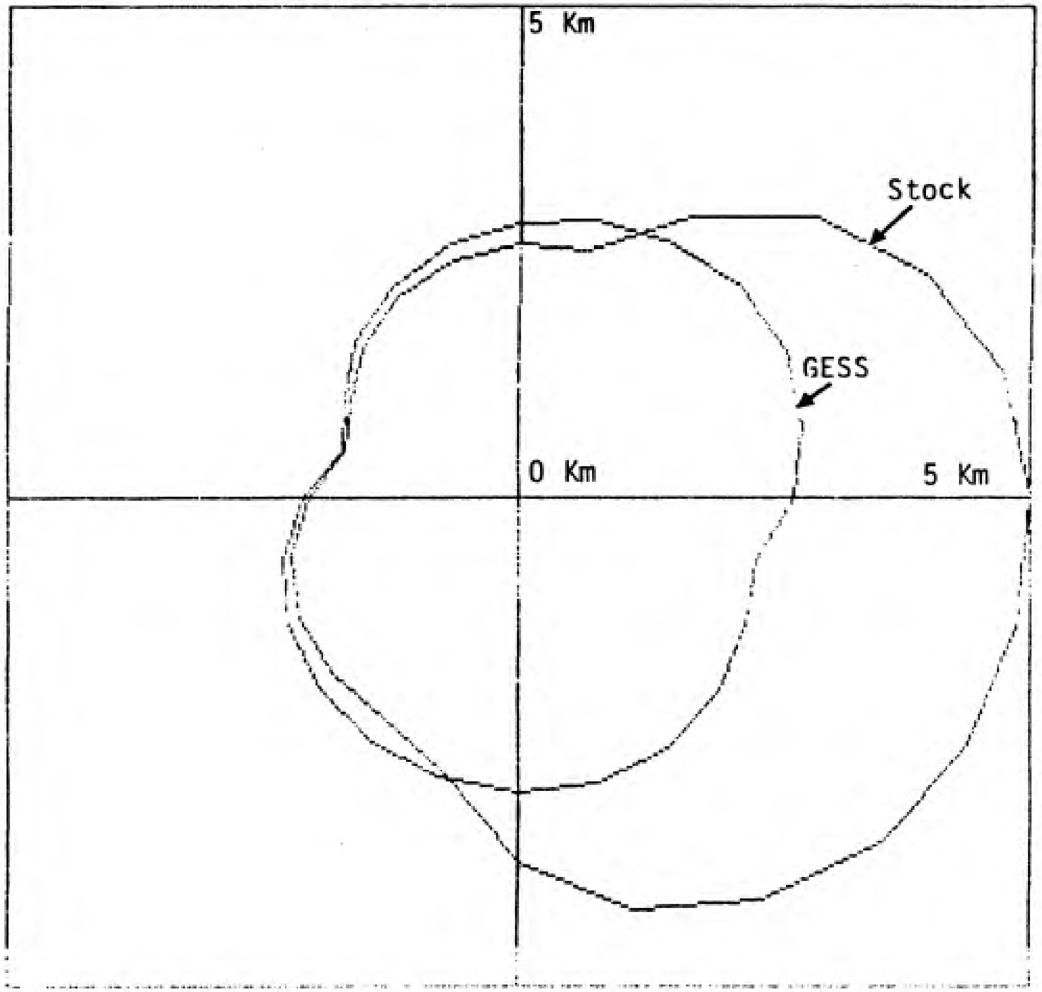

Figure A21. Baseline comparison with stock (no GESS) configuration. Noisy background, 0 Hr, 1-km sensor. Polar plot of detection range vs azimuth. North is up, east is right. All radial divisions are at 5-km intervals. Full scale = ± 5 km.

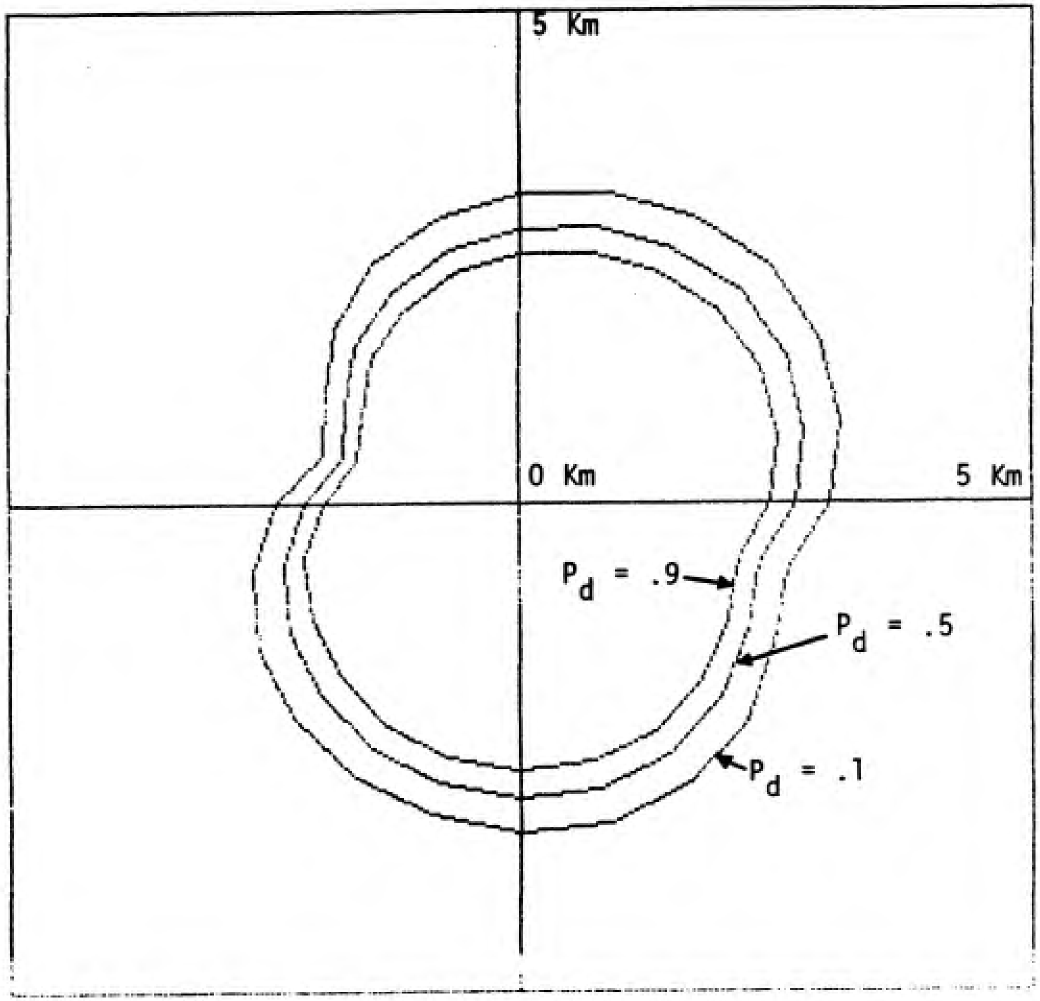

Figure A22. Baseline comparison with greater (.9) and lesser (.1) probability of detection. Noisy, 0 Hr. background, 1-km sensor. Polar plot of detection range vs azimuth. North is up, east is right. All radial divisions are at 5-km intervals. Full scale = ± 5 km.

The next parameter chosen for showing its importance is background clutter. Figure A23 illustrates the great effect this parameter can have on detection range. The lack of background structure presented by the Michigan winter forest compared to that of the AP Hill scene increases the detection ranges at many azimuths by 150 percent. This is a major effect and therefore must be included in the core camouflage comparisons.

The atmosphere through which the sensor views the target can be a major factor in certain circumstances. Under the specified conditions, however, it has a small effect. Figure A24 shows the change in detection envelopes caused by two extreme atmospheres--one of tropical 5-km visibility and one of midlatitude winter 23-km visibility. Under these conditions, atmospheric visibility is not a major factor, which is absolutely untrue for many target-sensor engagement scenarios; however, it has been shown to be inconsequential for the conditions of this study.

Another potentially significant parameter is that of sensor altitude. Figure A25 addresses this issue by presenting detection envelopes for sensor altitudes of .5, 1, and 2 km. Over this range of altitudes, detection ranges are again affected little.

Day-night variation is the last nontarget parameter of importance. Figure A26 illustrates the degree to which diurnal effects can alter the detection range. In considering this parameter, the importance of background structure is raised. In this example, although the target ΔT has increased substantially due to solar heating (see Table A2), the background thermal clutter has increased to a greater degree (see Table A5), so that, in fact, a target of larger ΔT has a lower detection range.

Clearly, then, the major parameters for studying camouflage material are diurnal variations and background clutter. For this reason, the remainder of the study is devoted to comparing different camouflage materials under extreme diurnal and background structure variations.

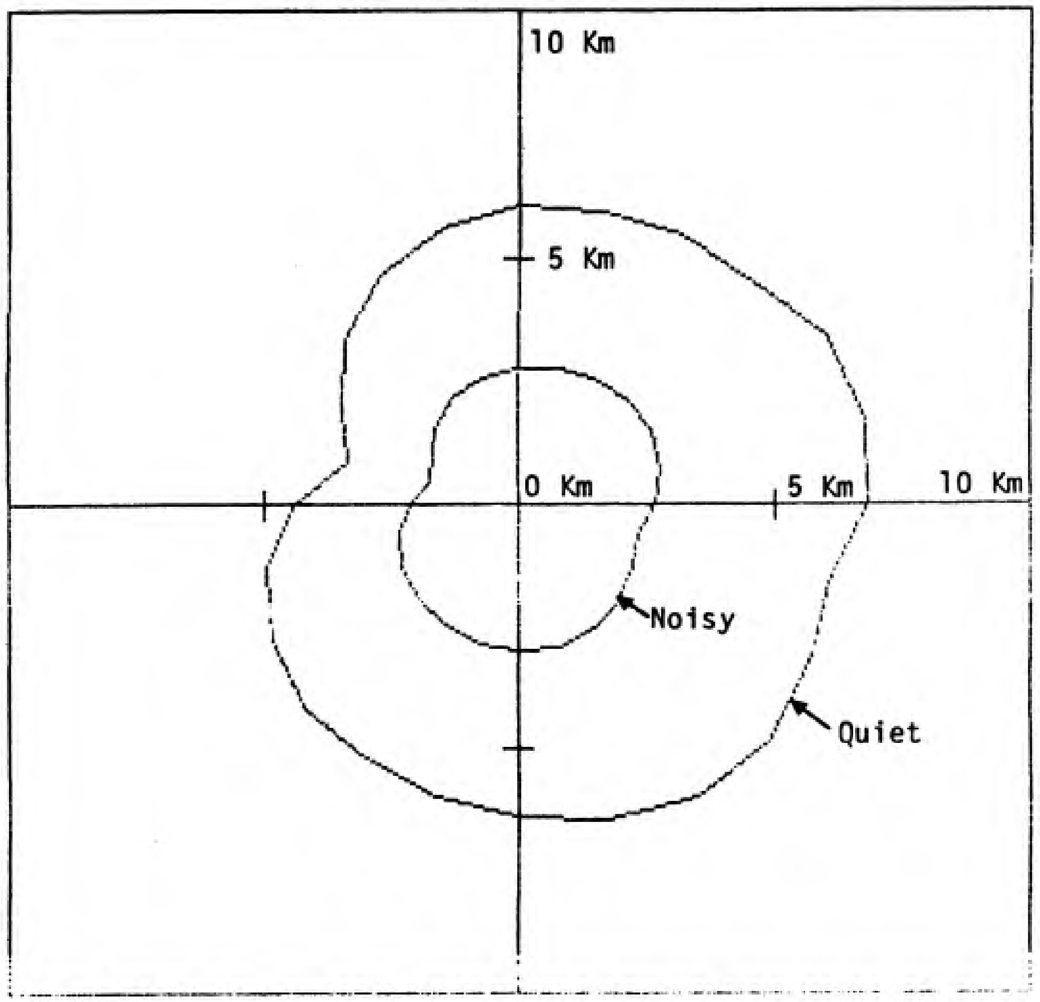

Figure A23. Baseline comparison with "quiet" Michigan conifer background, 0 Hr, 1-km sensor. Polar plot of detection range vs azimuth. North is up, east is right. All radial divisions are at 5-km intervals. Full scale = ± 10 km.

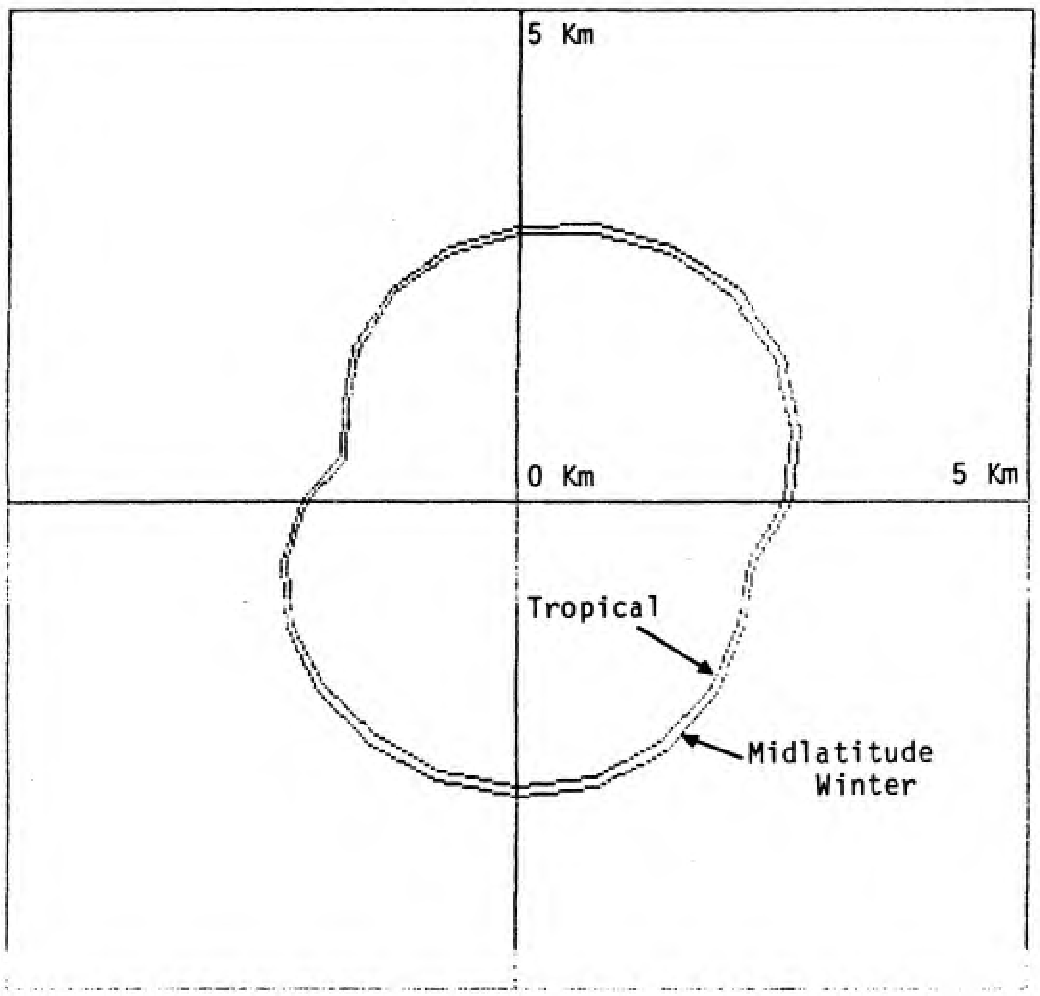

Figure A24. Baseline comparison with tropical atmosphere, 0 Hr, noisy background, 1-km sensor altitude. Polar plot of detection range vs azimuth. North is up, east is right. All radial divisions are at 5-km intervals. Full scale = ± 5 km.

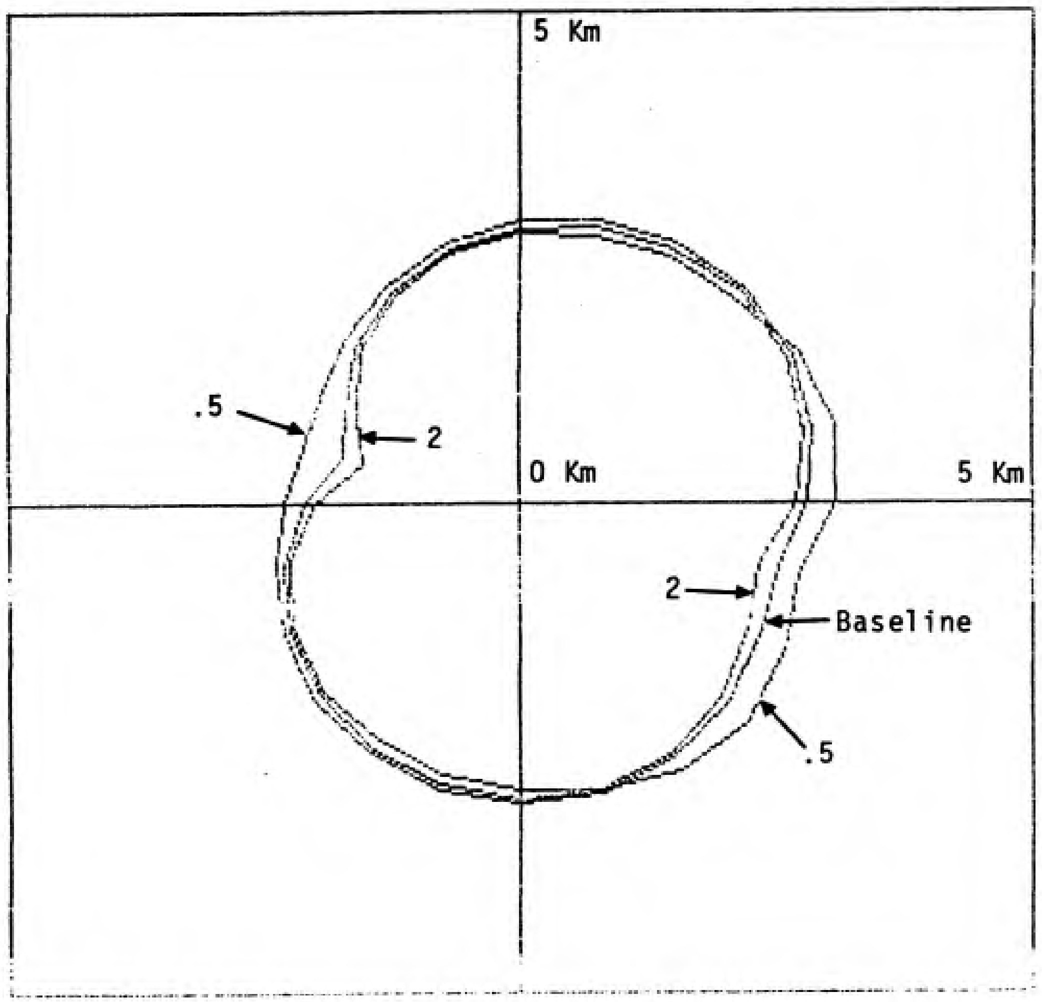

Figure A25. Baseline comparison with higher (2-km) and lower (.5-km) sensor altitude, noisy 0 Hr background. Polar plot of detection range vs azimuth. North is up, east is right. All radial divisions are at 5-km intervals. Full scale = ± 5 km.

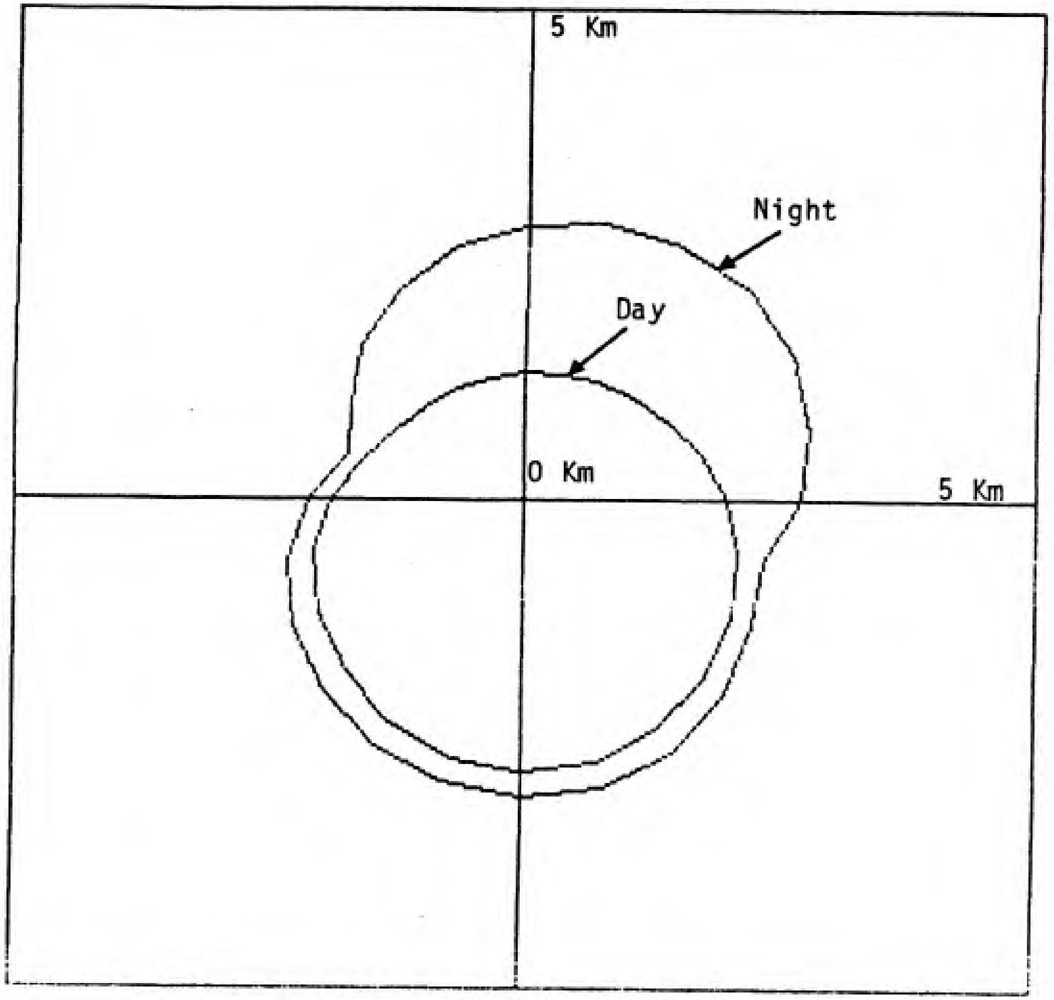

Figure A26. Baseline comparison with day, noisy background, 1-km sensor altitude. Polar plot of detection range vs azimuth. North is up, east is right. All radial divisions are at 5-km intervals. Full scale = ± 5 km.

Effectiveness of Candidate Systems

The comparison of the camouflage materials against the baseline case is presented in Figure A27. The configuration that displays the largest detection range, the aluminum-surfaced shell, performs badly, mainly because of the large negative ΔT values presented by the horizontal surfaces. As pointed out above, these apparent negative ΔTs result when these surfaces reflect the cold sky. These surfaces are the dominant contributors to large detection ranges; this fact is illustrated when these two facets are replaced with equivalent ones of bare foam to produce the so-called composite shell, which outperforms all other configurations in reducing the detection range. A shell made entirely of bare foam accomplishes the camouflage task to a degree, but cannot match the lower apparent ΔTs and detection ranges produced by the fairly reflective aluminum vertical facets.

It is important to remember that the ΔTs of the foam and composite shells are generally smaller than those of the 60-kw generator with GESS alone. However, the top is larger by nearly 20 percent, and the sides are larger by some 8 percent. The benefits of the shields would be more clear-cut if the shell could be made to fit tighter than the postulated 10-cm additional thickness (4 cm of foam plus 6 cm of space). Despite this penalty of increased surface area, the trend seen here generally persists for the remainder of the study. That is, the all-aluminum-surfaced foam shell usually performs worse than no shell at all, whereas the all-foam shell is somewhat better than no shell, with the composite shell displaying the best camouflage.

Figure A28 again shows this trend for the quiet night background. Here, all detection ranges have been increased in comparison to the noisy night background clutter noise. However, the relative performance of the four camouflage techniques remains the same. Again, the shell composed entirely of aluminum-surfaced foam performs the worst for most azimuths. However, the replacement of the two horizontal surfaces with equivalent ones of bare foam produces a camouflage shell that outperforms all other

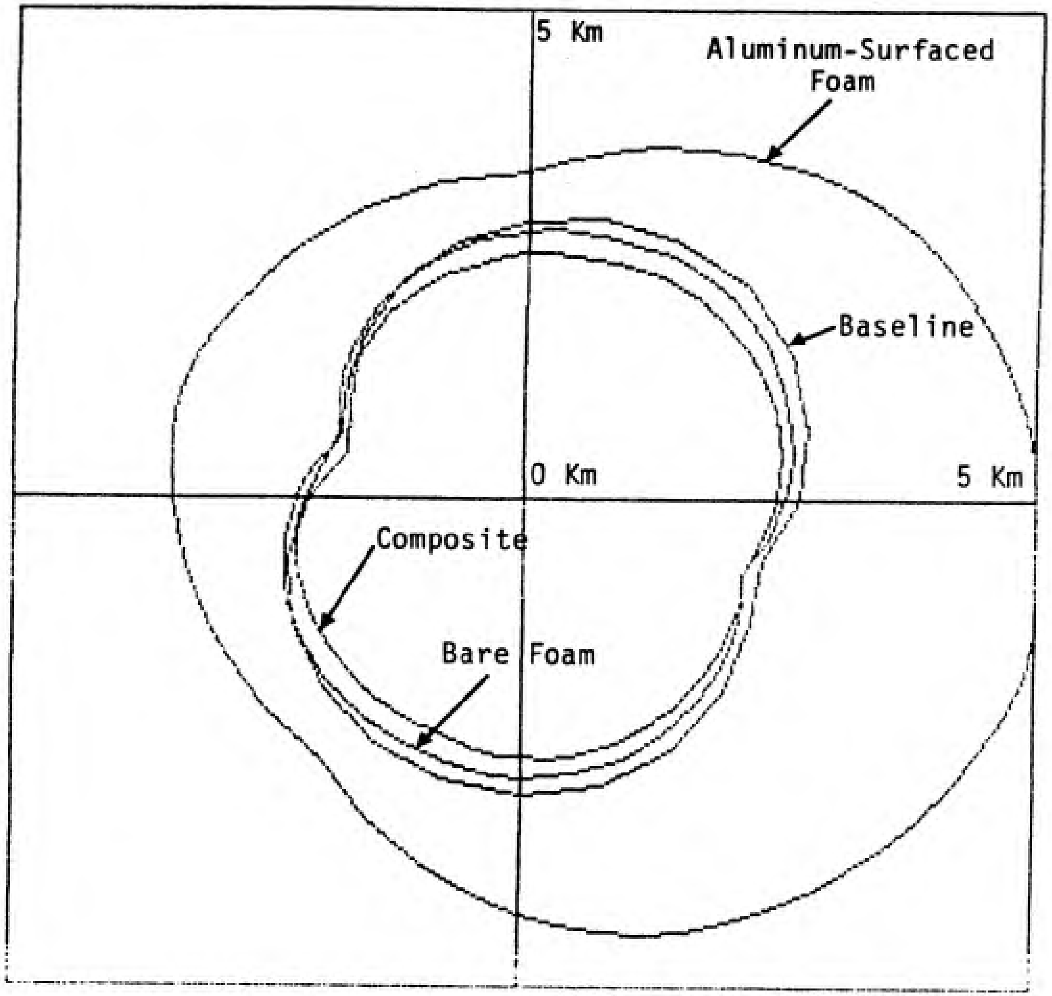

Figure A27. Baseline comparison with candidate shell designs: (1) foam, (2) aluminum-surfaced foam, and (3) composite foam and aluminum-surfaced foam. Noisy night background. Polar plot of detection range vs azimuth. North is up, east is right. All radial divisions are at 5-km intervals. Full scale = ± 5 km.

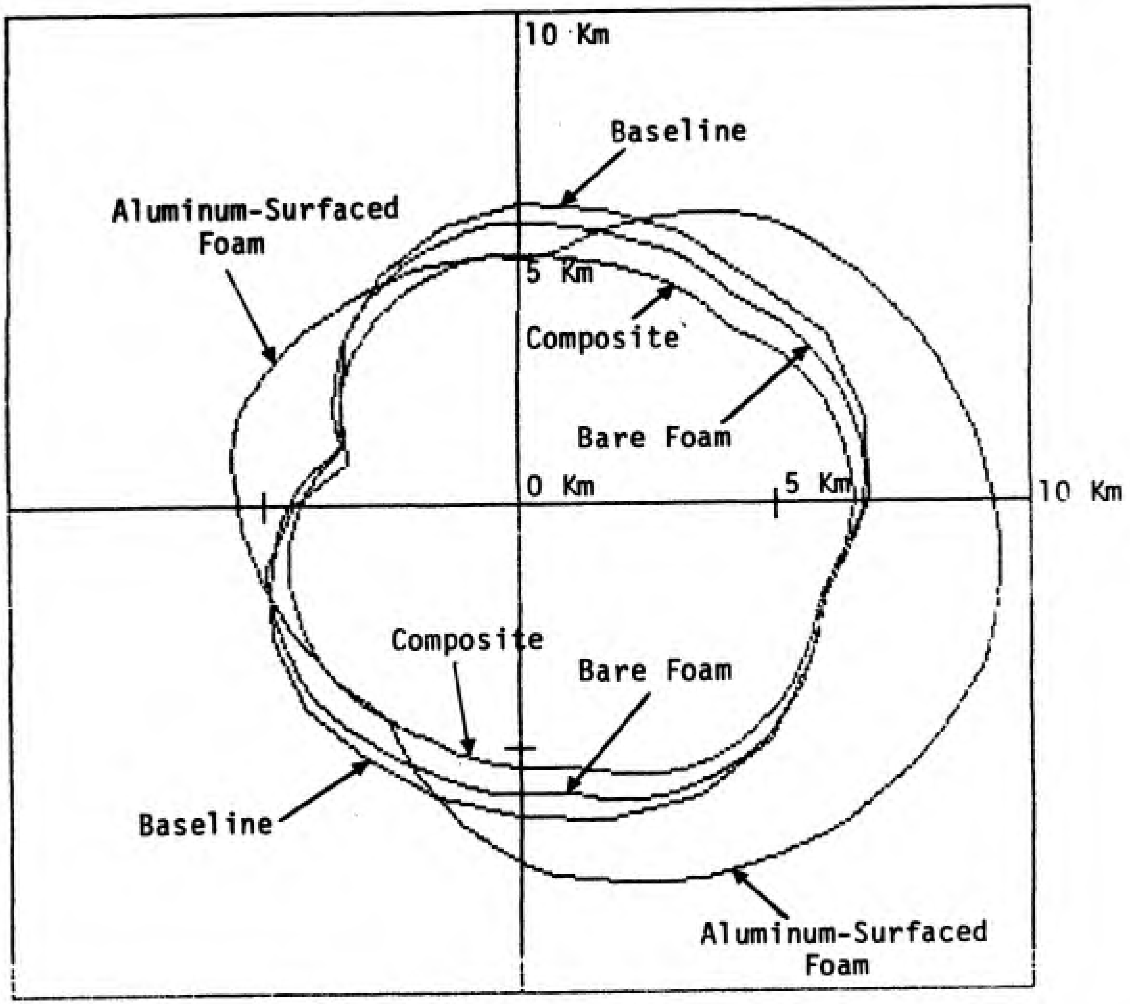

Figure A28. Baseline comparison with candidate shell designs: (1) foam, (2) aluminum-surfaced foam, and (3) composite foam and aluminum-surfaced foam. Quiet night background. Polar plot of detection range vs azimuth. North is up, east is right. All radial divisions are at 5-km intervals. Full scale = ± 10 km.

approaches. As in the noisy night case, the 100 percent bare foam shell reduced the detectability of the GESS-equipped 60-kw generator somewhat.

The daytime cases are both more complex and more clear-cut. Figure A29 illustrates the detection ranges for each of the four configurations. As seen previously, the all-aluminum-surfaced shell is the easiest to detect due to its large negative ΔT top surface. The foam shell, in contrast to the nighttime cases, now generally performs worse than no shell at all. The reason for the worse performance is that the insulating foam causes the surface to heat or cool in an essentially adiabatic manner--that is, with little regard to the interior temperature. The 60-kw diesel generator has a large volume of air being pulled through it, which heats only to a small degree in its passage through the enclosure; temperatures measured at the exhaust were never more than 30°C above ambient air even after passing through the radiator. This indicates that the temperature of the air circulating on the inside of the walls before passing through the radiator is only somewhat warmer than ambient. For this reason, the side and top walls of the generator enclosure do not show large ΔTs with respect to the background. The sunlit sides are cooled from within, whereas the shadowed sides are warmed by the same mechanism.

In contrast, the foam shell heats on the sunlit side with no heat flux to the interior, and the shaded side cools nearly 10° with respect to the background. Thus, the foam shell increases the magnitude of the apparent target ΔTs during the day. This situation is greatly improved by adding the reflective aluminum surface to the foam for the side panels. As discussed previously, the foil surface reduces the apparent ΔT by reflecting the background, thus reducing the detection range by 40 percent for most of the southern side. There are straightforward corrections for the vulnerability still presented by the shaded, northern side; these will be discussed in the conclusions.

The quiet day case shown in Figure A30 completes the parametric analysis of the study. Here again is the relative performance exhibited by the noisy daytime background, augmented by the reduced clutter in the Michigan conifer background.

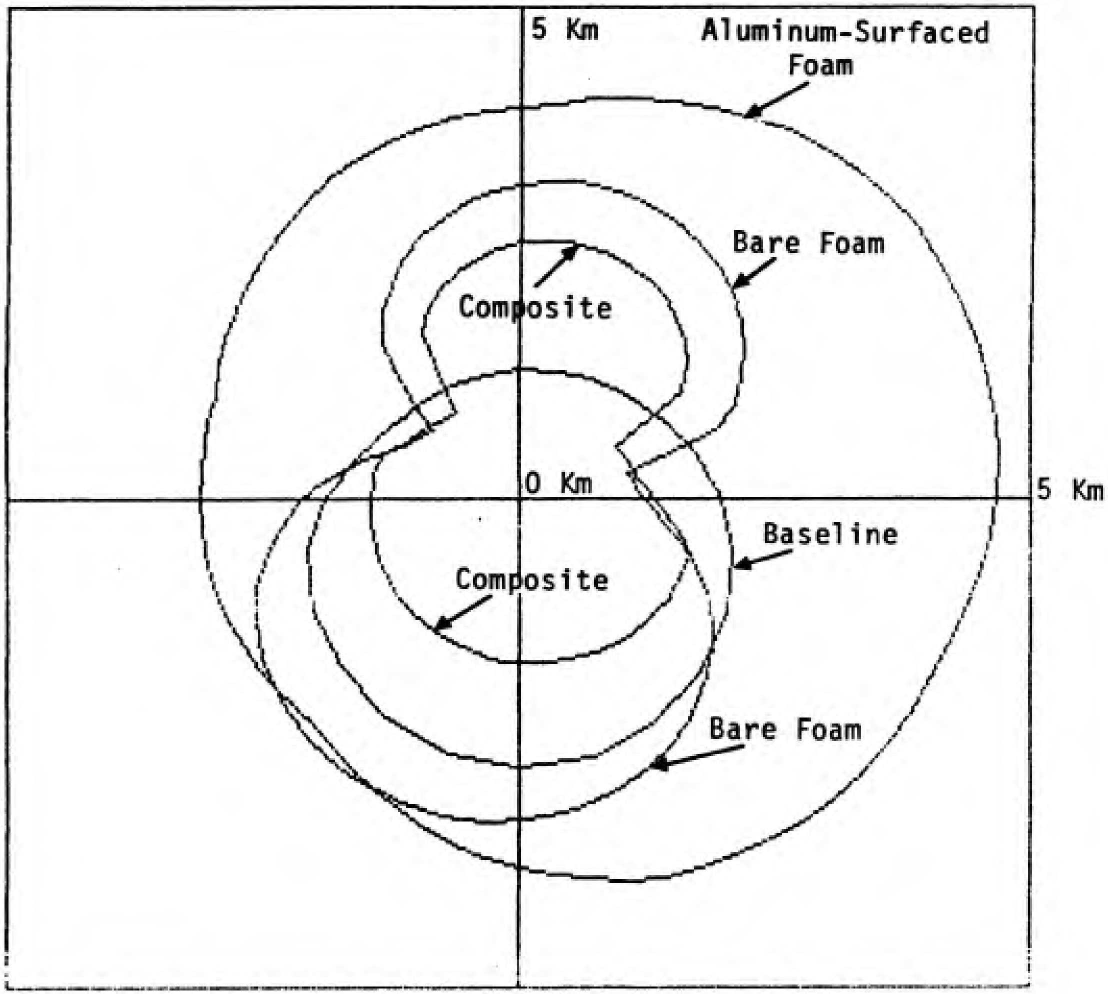

Figure A29. Baseline comparison with candidate shell designs: (1) foam, (2) aluminum-surfaced foam, and (3) composite foam and aluminum-surfaced foam. Noisy day background. Polar plot of detection range vs azimuth. North is up, east is right. All radial divisions are at 5-km intervals. Full scale = ± 5 km.

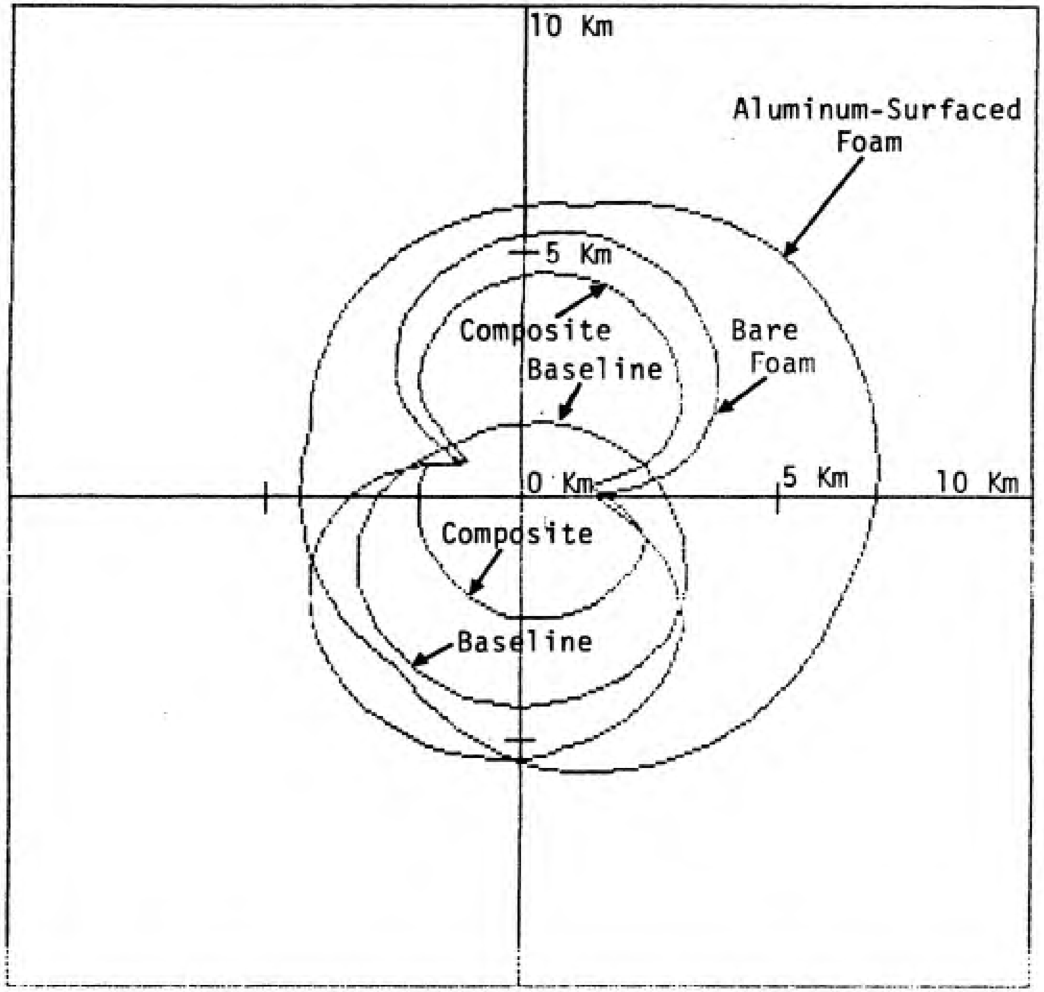

Figure A30. Baseline comparison with candidate shell designs: (1) foam, (2) aluminum-surfaced foam, and (3) composite foam and aluminum-surfaced foam. Quiet day background. Polar plot of detection range vs azimuth. North is up, east is right. All radial divisions are at 5-km intervals. Full scale = ± 10 km.

6 CONCLUSIONS

The basic attribute of the foam material is that it can isolate the interior and exterior surfaces of an enclosure. This property is both a benefit and a hindrance. Insulated adiabatic surfaces exhibit a wider range of temperatures than most backgrounds, which causes the greater vulnerability of the foam-shell-covered unit than that of the baseline during the day.

One possible way to solve this problem would be to create a surface for which the thermal time constant and mass equaled those of the background. This task could be accomplished using exotic materials, but such an approach is unattractive in terms of cost and practicality. Far more appealing is the use of a specular, highly reflective coating for the sides such as that offered by aluminum-surfaced foam panels. When used only on the sides, this material provides very desirable camouflage qualities. On the other hand, this foil coating <u>should</u> <u>not</u> be used on horizontal surfaces because of the large negative contrast it produces by reflecting the cold sky back to observers.

It should be pointed out that the 60-kW diesel generator with GESS is not an extremely detectable unit, and, as such, does not show dramatic order-of-magnitude improvements by the application of even the composite shell. Because of the large volume of air being pulled through the enclosure, it rarely shows ΔTs larger than 3 or 4°C. This would not be the case for a target with no thermal regulator. For instance, it is not uncommon for tanks or trucks to exhibit ΔT values larger than 20°C; such units would benefit much more by the application of bare foam shells than the generator considered in this study.

One conclusion derived from the current study is that each of the materials is potentially useful for camouflage applications. The best camouflage is obtained by an enclosure with perfectly reflective sides and a top which, by active or passive means, undergoes the same temperature cycle as the background. The composite shell approaches this goal. The sides are nearly 50 percent reflective in the 8-12 μm region, and the bare foam horizontal surfaces do not display large ΔTs. However, this combination does little better than the generator alone with its internally circulated air.

Significant improvements can be obtained by increasing the side panels' reflectivity. Increased reflectance of these side surfaces would simultaneously reduce the insulation requirement.

The issue of the top surface is more difficult to address. It can easily be stated that one should seek a coating that mimics the spectral properties of the background and that, furthermore, shows the same thermal dynamics as the background. In fact, neither the baseline nor the foam shell behave very badly in comparison to this ideal. At the peak solar loading period, neither is off more than 4°C from the background temperature. Until high performance systems are developed, it probably is not worth a great deal of effort to obtain daytime ΔTs on the order of 1°C or less, unless the sensor can be vectored to the target location by other means, or the target is large. Some effort, however, could be made to reduce the bare foam daytime ΔTs by increasing the visible reflectance and thermal emission.

In conclusion, it should be stated that CERL's proposed camouflage material provides a substrate with which camouflage engineers can work productively. The bare foam surface could be improved by reducing its tendency to solar-heat, whereas the aluminum-surfaced foam could be improved by increasing its reflectivity. The aluminum-surfaced material should never be used as a top surface, but this material certainly has potential as a camouflage.

REFERENCES

LaRocca, A.J., and D.J. Witte, Handbook of the Statistics of Various Terrain and Water (Ice) Backgrounds from Selected U.S. Locations, ERIM Report No. 139900-1-X (1980).

Rice, S.O., "The Mathematical Analysis of Random Noise," Bell Sys. Tech. J. Vol. 23 (1944), pp. 282-332; Vol. 24 (1944), pp. 146-156.

TCATA/3rd Corps Field Test. Data made available by Dr. Gandy, Fort Hood, TX.

Zimmerman, D.M., Impact of Advanced Detection Algorithms on Camouflage Requirements, PRA Deliverable, Contract No. DAAK70-79-C-0098 (January 1981).

SPECIAL DISTRIBUTION

Chief of Engineers

ATTN: DAEN-ASI-L (2)
ATTN: DAEN-CCP
ATTN: DAEN-CW
ATTN: DAEN-CWE
ATTN: DAEN-CWM-R
ATTN: DAEN-CWO
ATTN: DAEN-CWP
ATTN: DAEN-EC
ATTN: DAEN-ECC
ATTN: DAEN-ECE
ATTN: DAEN-ZCF
ATTN: DAEN-ECR
ATTN: DAEN-RD
ATTN: DAEN-RDC
ATTN: DAEN-RDM
ATTN: DAEN-RM
ATTN: DAEN-ZCZ
ATTN: DAEN-ZCE
ATTN: DAEN-ZCI
ATTN: DAEN-ZCM

FESA, ATTN: Library 22060
ATTN: DET III 79906

US Army Engineer Divisions
ATTN: Library (14)

US Army, Fort Belvoir 22060
ATTN: Engr Topographic Lab
ATTN: R&D Center
ATTN: ATZA-CDC

CRREL, ATTN: Library 03755

WES, ATTN: Library 39180

Tyndall AFB, FL 32403
AFESC/Engineering & Service Lab

NCEL 93041
ATTN: Library (Code L08A)

Smith, Alvin
An investigation into polymer design and synthesis for infrared energy absorption.--Champaign, Ill : Construction Engineering Research Laboratory ; 1984.
81 p (Technical report ; M-345)

1. Infra-red rays. 2. Polymers and polymerization. 3. Plastic foams. I. Title. II. Series: Technical report (Construction Engineering Research Laboratory) ; M-345.